Dissecting a biological electron transport network with electrochemistry

Joshua M. Lawrence[1,2], Rachel M. Egan[2], Laura T. Wey[3], Karan Bali[4], Xiaolong Chen[5], Darius Kosmützky[1], Mairi Eyres[2], Lan Nan[2], Mary H. Wood[6], Marc M. Nowaczyk[7], Christopher J. Howe[1,*], Jenny Z. Zhang[2,*]

1 Department of Biochemistry, University of Cambridge, Cambridge, UK
2 Yusuf Hamied Department of Chemistry, University of Cambridge, UK
3 Molecular Plant Biology, Department of Life Technologies, University of Turku, Turku, Finland
4 Department of Chemical Engineering and Biotechnology, University of Cambridge, Cambridge, UK
5 Department of Mechanical, Materials and Manufacturing Engineering, University of Nottingham, Nottingham, UK
6 Niels Bohr Institute, University of Copenhagen, Copenhagen, Denmark
7 Department of Biochemistry, University of Rostock, Rostock, Germany

Abstract

Electron transport chains (ETCs) drive fundamental biological processes, including respiration and photosynthesis. Methodology for studying biological electron transport on a systems-level is lacking, owing to ETCs forming complex overlapping networks of electron transfer, akin to cellular metabolism. Here, we demonstrate the use of electrochemistry to study the highly complex electron transport found in the thylakoid membranes of cyanobacteria. By interfacing thylakoid membranes with highly structured electrodes, we revealed electrochemical signatures originating from the direct electron transfer (DET) between membrane components and the electrode. Analysis of these signatures enabled the measurement and disentanglement of respiratory and photosynthetic signals, with results exhibiting consistency with biophysical measurements of ETC activity. These findings establish natural membrane electrochemistry as a useful tool for investigating biological electron transport from the scale of individual proteins to entire ETCs, with immediate applications in analysing membrane bioenergetics and guiding the design of biohybrid energy-conversion technologies.

Introduction

The membrane-localised ETCs of living organisms can drive a diverse array of respiratory and photosynthetic processes, thereby acting as the primary agents of energy flow in ecosystems whilst also driving much of the Earth's geochemical cycles[1]. Furthermore, the catalytic activities of electron transport chains can be harnessed by researchers developing biohybrid devices for the sustainable generation of electricity, fuels and high-value chemicals[2,3]. It is therefore essential to create tools that help us to understand the molecular mechanisms underpinning the function of electron transport chains.

Analysis of electron transport chains is often complicated by the fact that they include various bifurcating pathways and catalytic processes, whilst utilising many different redox proteins and cofactors[1,2,4–6]. Many organisms contain multiple electron transport chains within the same membrane, with these pathways often sharing components or catalysing coupled or opposing chemical reactions[7–14]. Furthermore, organisms have evolved a variety of mechanisms to regulate the activity of electron transport chains in response to environmental conditions, to ensure their correct functioning and prevent the generation of cytotoxic reactive oxygen species[15–22]. Biological electron transport can therefore be understood as a network, the complexity of which limits our ability to analyse the activity or function of specific pathways or their interplay with other pathways. Research has largely focused on characterisation of purified redox proteins *in vitro*[23–27], spectroscopic analysis of highly-expressed redox proteins *in vivo*[19,28–32], or indirect measurements on the impact of electron transport processes on cell growth and physiology[33–37]. Few analytical tools exist which can provide a systems-level understanding of electron transport chain activity, whilst also being applicable to a wide variety of biological membranes.

Analytical electrochemistry has been widely applied to purified redox proteins and other biomolecules to analyse the kinetics and dynamics of their electron transfer reactions[24,27,38], albeit in a non-native environment. Similar techniques have also been applied to cultures and biofilms of diverse microorganisms[39–49], revealing complex electrochemical signatures. Although these signatures are information-rich and relate directly to the photosynthetic or respiratory activity of the cells, they are difficult to analyse[50]. Bioelectrochemical analysis of natural membranes could mitigate these trade-offs, enabling a systems-level analysis of the complex electron transport networks existing within these membranes.

Herein, we demonstrate the direct electrochemical analysis of the photosynthetic thylakoid membranes of cyanobacteria (Fig.1a)- an ancient, diverse and ubiquitous phylum of photosynthetic bacteria[51,52] which contribute ~25 % of total primary photosynthetic productivity[53]. Their intracellular and multilamellar thylakoid membranes host the linear photosynthetic electron transport (LET) chain, which uses solar energy to couple water oxidation to the synthesis of energy carrier molecules[7,54]. In addition, cyanobacterial thylakoid membranes contain various cyclic photosynthetic electron transport (CET) pathways, as well as a complete respiratory electron transport (RET) chain[7,55]. A typical RET is not found in the thylakoid membranes of plant and algal chloroplasts, as respiration is performed in the mitochondria of these organisms[6]. Their variety of electron transport chains makes cyanobacterial thylakoid membranes some of the most protein dense in nature[56], with perhaps the most complex network of interdependent electron transport pathways (Fig. 1b).

Photosynthetically active thylakoid membrane vesicles were isolated from cyanobacteria and interfaced with highly structured electrodes, enabling sensitive photoelectrochemical measurements of thylakoid membrane to be performed (Fig. 1a). Analysis of the observed photoelectrochemical signals allows for the study of the highly complex biological electron transport network found within these membranes (Fig. 1b), without requiring protein purification whilst overcoming the inability of spectroscopic methods to distinguish between processes with similar spectroscopic profiles.

Results

Wiring thylakoid membranes to electrodes:

Previous methods for crude cyanobacterial thylakoid membrane extraction[49,57] were adapted to isolate enriched thylakoid membranes from the model cyanobacterium *Synechocystis* sp. PCC 6803 (Extended Data Fig. 1a and Methods). Based on measurements of chlorophyll (chl) *a* concentration, this thylakoid membrane isolation method enabled ~33% of the thylakoid membrane to be recovered, yielding vesicles with a diameter of 100-250 nm, as measured by electron microscopy (Fig. 1e) and nanoparticle tracking analysis (Extended Data Fig. 1b), with polymer 2-phase separation[58] revealing a preferential orientation with the cytoplasmic face outwards in 84.3±2.5% of vesicles. Thylakoid membrane samples exhibited clear absorbance and fluorescence signatures for chl *a* but lacked those for phycobilisomes, many of which detached from the membranes during extraction (Extended Data Fig. 1c-d and Supplementary Fig. 1a). However, SDS-PAGE analysis showed the presence of bands characteristic of the phycobiliproteins CpcA/B in thylakoid membrane samples (suggesting some phycobilisomes remain attached), alongside other bands corresponding to thylakoid membrane proteins[59] (Supplementary Fig. 2). BN-PAGE demonstrated the presence and integrity of major thylakoid membrane complexes in the samples (Extended Data Fig. 1e), consistent with results from previous studies[60]. A suite of methods was used to demonstrate the functioning of the entire LET in isolated thylakoid membranes, although no light-dependent proton motive force could be measured, suggesting the vesicles were permeable to small ions (Extended Data Fig. 2 and Supplementary Note 1).

To enable high loading and efficient wiring of isolated thylakoid membranes to electrodes, hierarchically structured and translucent inverse opal-indium tin oxide (IO-ITO) electrodes[48] were fabricated with a pore diameter of 10 µm and solvent channel diameter of 2 µm (Extended Data Fig. 3a-b), enabling thylakoid membrane vesicles to penetrate the electrode structure. Thylakoid membrane-modified IO-ITO electrodes were created by dropcasting a thylakoid membrane suspension onto a bare electrode, leading to the formation of a multi-membrane thick layer of thylakoid membranes coating the ITO-nanoparticles throughout the electrode structure (Fig. 1c-d and Extended Data Fig. 3c). QCM-D measurements of thylakoid membrane adsorption to ITO-coated chips revealed a large monophasic decrease in frequency and increase in dissipation (Extended Data Fig. 3d), consistent with the adsorption of vesicles to the ITO without the formation of any structured lipid bilayer at the electrode surface[61].

Photocurrent measurements of thylakoid membrane-modified IO-ITO electrodes under moderate red light (50 µmol photons m^{-2} s^{-1} at 680 nm) were performed in chronoamperometry experiments using a photoelectrochemical cell (Extended Data Fig. 4a and Supplementary Fig. 4a) with data analysis performed with bespoke software (Extended Data Fig. 4b, Methods and Supplementary Note 2). Notably, thylakoid membranes exhibited a distinct photocurrent profile consisting of a sharp spike in current in the dark-light transition, followed by relaxation to a steady state light current, with a rapid return to the steady state dark current following a light-dark transition (Fig. 1f). These photocurrent profiles features are different from those observed from photocurrent measurements of individual photosystems (which are monophasic) or of cyanobacterial biofilms (which have more complex profiles)[48,49], leading us to hypothesise that they encode information about the dynamics of electron transport within the isolated thylakoid membranes. The features were quantified as two parameters: (i) the 'Spike Charge' (the total charge contained within the initial spike feature); and (ii) the

'Steady State Photocurrent' (the positive difference in current between the light and dark steady states. This enabled quantitative analysis of these parameters under different experimental conditions.

Experimental conditions were optimised to enable thylakoid membrane photocurrents to be recorded in physiologically relevant conditions. As expected, increased loadings of thylakoid membranes onto electrodes yielded enhancements in both the Spike Charge and Steady State Photocurrent (Extended Data Fig. 5a) albeit at different rates, with Steady State Photocurrents plateauing with 10 µg of chl *a* and Spike Charges continuing to increase at 20 µg of chl *a*. This is consistent with the Steady State Photocurrents being caused by DET to the electrode, which reaches its maximum when the electrode surface is completely covered with thylakoid membranes (Extended Data Fig. 3c and Supplementary Fig. 3); with Spike Charges instead stemming from currents (either non-Faradaic and/or Faradaic) caused by mobile charged species trapped within the isolated thylakoid membrane samples. Recording photocurrents under increasing intensities of 680 nm light showed a clear light-dependent enhancement in the Steady State Photocurrent, which was not observed for the Spike Charge (Extended Data Fig. 5b). The effect of pH, ΔpH, buffer, oxygen and sample degradation on photocurrent parameters were also determined (Extended Data Fig. 5c-g and Supplementary Note). This led to the selection of standard, physiologically relevant experimental conditions for use in subsequent thylakoid membrane electrochemistry experiments (Methods and Supplementary Note 3).

Probing photosynthetic electron transport pathways:

The different dependencies of the Steady State Photocurrent and Spike Charge on chl *a* loading, light intensity and pH (Supplementary Note 3 and Extended Data Fig. 5a-c) suggest that these two photocurrent parameters originate from different electron transport pathways between thylakoid membrane components and the electrode. This makes it hard to ascertain the dependence of these parameters on the LET, which *in vivo* begins with water oxidation and photoexcitation by photosystem II (PSII), ending with the synthesis of the redox carrier NADPH following an additional photoexcitation performed by photosystem I (PSI; Fig. 2a). To probe the contribution of the LET to photocurrent profile parameters, photocurrents were recorded in the presence of different chemicals (biomolecules, inhibitors, artificial electron mediators), light conditions and working electrode potentials (E_{app}) to elucidate and discriminate between electron pathways from the PETC to the electrode. As a rule-of-thumb (based on Marcus theory and experimental measurements), redox cofactors can be assumed capable of performing DET to the electrode if they lie within 2 nm of the cytoplasmic face of a thylakoid membrane which contacts ITO[62]. The structures of the major photosynthetic complexes in simulated lipid bilayers[63] suggest that multiple redox cofactors lie within this range: Q_A and Q_B of PSII; haem c_n of cytochrome b_6f; PhQ, Fe_X, Fe_A and Fe_B of PSI (Extended Data Fig. 6). Previous publications have shown the ability of an electrode to oxidise plastoquinol (PQH_2) within a lipid bilayer into plastoquinone (PQ) directly, albeit at a large overpotential[64].

Titrations of several PETC inhibitors were performed to determine their inhibition of thylakoid membrane photocurrent parameters relative to a control titration of DMSO (Fig. 2b). DCMU, a competitive inhibitor of the PSII Q_B site[65], provided a strong inhibition of Steady State Photocurrent up to 93% but had no inhibitory effect on the Spike Charge, suggesting that whilst Steady State Photocurrent is PSII-dependent, Spike Charge is purely PSI-dependent. DCMU also provided a small enhancement in the Spike Charge, although this could be caused by the signal from the Steady State Photocurrent feature occluding the spike feature. HQNO, is a competitive inhibitor of the cytochrome b_6f Q_n site[66], and is thought to prevent electron transfer downstream of haem b_n, thereby disrupting the Q-cycle without affecting the high potential chain of cytochrome b_6f which transports electrons to PSI via plastocyanin[67]. HQNO was not observed to inhibit the Spike Charge consistent with this feature being PSI-dependent, whilst a 74% inhibition of the Steady State Photocurrent suggests that a sizeable proportion of this feature originates from direct electron transfer between cytochrome b_6f and the electrode. PMA, which inhibits ferredoxin electron transfer[68], did not provide a greater inhibition of Steady State Photocurrent or the Spike Charge than the DMSO control. This suggests ferredoxin does not act as an electron mediator between PSI and the electrode, consistent with ferredoxin being lost during thylakoid membrane isolation (Extended Data Fig. 2f and Supplementary Note 1) and PSI performing electron transfer to the electrode. Photocurrents recorded with actinic light at longer wavelengths (700 and 730 nm) which selectively excite PSI over PSII[69], further showed the PSI-dependent nature of the Spike Charge in comparison to the Steady State Photocurrent (Fig. 2c and Supplementary Fig. 6).

Stepped chronoamperometry experiments (in which photocurrents were recorded at increasing E_{app} values) were performed, with the onset potential (most negative potential when Faradaic features appear) used to distinguish between electron transfer from different PETC redox cofactors to the electrode (Fig. 2d-e). Enzymatic oxygen removal was used in these experiments to expand the range of accessible E_{app} values with ITO electrodes to -600

mV vs standard hydrogen electrode (SHE)[70]. An onset potential for anodic photocurrents was observed at -100 mV vs SHE, with the Steady State Photocurrent reaching its maximum at +100 mV vs SHE, consistent with the feature being dependent on DET from PSII and cytochrome b_6f to the electrode[2,48]. A fast decline in the Spike Charge was observed at E_{app} > +300 mV vs SHE, which can be explained by the oxidation of PQH_2 by the electrode[64] (see below) competing with reduction of the PSI reaction centre P700. The ferri-/ferrocyanide redox couple has an E_m of +420 mV vs SHE (Supplementary Fig. 7); below this potential it acts as an electron donor to PSI[71], and above this as an electron acceptor from PSII and cytochrome b_6f[72,73]. Addition of this molecule led to an onset of anodic photocurrents with a clear spike feature at E_{app} values as low as -600 mV vs SHE (Supplementary Fig. 8), an onset potential that can only be explained by DET from either PhQ or Fe_X of PSI to the electrode[2]. This onset potential for PSI photocurrents is, to our knowledge, more negative than any other previously measured in the literature, probably owing to decreased charge recombination caused by the favourable orientation of PSI in the thylakoid membrane with the cytoplasmic side interfacing with the electrode[74,75]. However, we cannot discount the possibility that mediated electron transfer from PSI to the electrode occurs at more positive E_{app} values. At E_{app} values ≥ +500 mV vs SHE a clear enhancement in the Steady State Photocurrent was observed, caused by ferricyanide mediation from PSII to the electrode. In this condition the Spike Charge disappeared entirely- consistent with the Steady State Photocurrent being caused by PSII- and cytochrome b_6f-dependent electron transfer and the Spike Charge by PSI-dependent electron transfer (Fig. 4a).

Soluble redox proteins and metabolites are expected to have been depleted during thylakoid membrane isolation, especially those located within the cytoplasm such as ferredoxin and NADP(H)[7]. To test the effect of this depletion, photocurrents were recorded in electrolyte exogenously supplemented with the soluble fraction obtained during thylakoid membrane isolation (Extended Data Fig. 1a). Soluble fraction addition led to the onset potential of anodic photocurrents being shifted to -400 mV vs SHE (Extended Data Fig. 7a and Supplementary Fig. 9), suggesting that its addition stimulated PSI-dependent electron transfer to the electrode. Lower onset potentials were also observed with soluble fraction passed through a 3 kDa cut-off filter to remove redox proteins such as ferredoxin, but no significant enhancement in Steady State Photocurrent or Spike Charge versus control measurements was observed with soluble fractions at E_{app} ≥ 0 mV vs SHE (Extended Data Fig. 7b). Cyclic voltammetry of soluble fraction revealed the presence of a small redox molecules with an E_m of +53 mV vs SHE (Extended Data Fig. 7c), which is too positive for this species to be enhancing photocurrents at low E_m values by acting as an electron mediator. Fluorescence analysis revealed the presence of phycobilisomes in soluble fraction, alongside the presence of metabolites with blue fluorescence (Extended Data Fig. 7d and Supplementary Fig. 1b). NADPH was shown to exhibit this same fluorescence peak (Extended Data Fig. 8a and Supplementary Fig. 1c), with cyclic voltammetry showing that NADP(H) could not act as an electron mediator over the tested E_m range (Extended Data Fig. 8b). Titration of NADPH into the electrolyte led to an enhancement of the Spike Charge at concentrations ≥ 500 µM (Extended Data Fig. 8c), suggesting the lower onset potential provided by soluble fraction may be caused by NADPH-dependent reduction of the P700 reaction centre of PSI via CET and RET pathways[7] (see below). The same effect was observed with $NADP^+$ addition (Extended Data Fig. 8d), consistent with the NADPH generation in the dark observed in spectroscopy experiments (Extended Data Fig. 2f and Supplementary Note 1). These data suggest that the Spike Charge of photocurrent profiles recorded under standard conditions (Fig. 1f) can be attributed to diffusible electron donors (as opposed to electron acceptors) being present in the sample, with the increase of the Spike Charge at high loadings (Extended Data Fig. 5a) being caused by the addition of electron donors trapped within the thylakoid membrane vesicles. Interestingly, the addition of soluble fraction and NADPH introduced a new feature in the photocurrent profile also- a transient decrease in the current occurring at light-dark transitions (Supplementary Fig. 9 and 11a-b). Further experiments are required to understand the molecular mechanisms underpinning this electrochemical signature.

To identify the redox cofactors responsible for electron transfer to the electrode, stepped chronoamperometry was performed in the presence of inhibitors. Inhibition of the Steady State Photocurrent was only observed at E_{app} values of ≥ +100 mV vs SHE for DCMU and ≥ +200 mV vs SHE for HQNO (Fig. 2f), consistent with electron transfer from PSII Q_B and cytochrome b_6f haem c_n with the electrode (Fig 4a). Cyclic voltammetry of thylakoid membranes performed in the absence and presence of these inhibitors revealed a series of different oxidation and reduction peaks (Extended Data Fig. 9a-b), demonstrating that multiple thylakoid membrane redox cofactors were interfaced with the electrode. One pair of peaks, E^1_{Ox} and E^1_{Red} both exhibited a positive shift in potential in the presence of DCMU suggesting they originate from the same cofactor with an E_m of +77 mV vs SHE (Extended Data Fig. 9c). $PQ(H_2)$ is known to have two distinct E_m values depending on whether it is protein-bound within PSII as the cofactor Q_B or free within the membrane PQ pool, with the latter having a more positive E_m[2]. Not only is the E_m of this cofactor consistent with either Q_B or $PQ(H_2)$[2], but the positive shift in potential in the presence of DCMU (and not HQNO) could be caused by displacement of Q_B by the inhibitor,

leading to its conversion into $PQ(H_2)$[76]. The presence of these redox peaks thereby demonstrates DET between the thylakoid membranes and the electrode. This $PQ(H_2)$ Oxidation of the PQ pool by the electrode could disrupt electron transfer from PSII to PSI (Fig. 2a). To test this, photocurrents were recorded following a pre-treatment with either 500 µmol photons m^{-2} s^{-1} of 680 nm light (to promote PQ pool reduction by PSII), or 50 µmol photons m^{-2} s^{-1} of 730 nm light (to promote PQ pool oxidation by PSI) (Supplementary Fig. 10). A 3.5-fold enhancement in the Spike Charge was observed in the former condition, with DCMU abolishing this enhancement (Fig. 2g). This demonstrates how PSII activity enhances PSI-dependent electron transfer to the electrode, thereby proving functional electron transport along the LET chain in isolated thylakoid membranes interfaced with the electrode (Fig. 4a).

Probing respiratory and cyclic electron transport pathways:

The finding that the Spike Charge is linked to both the NADPH concentration (Extended Data Fig. 8c) and the PQ pool redox state (Fig. 2g), suggests the spike feature is caused by an accumulation of reduced P700 in the dark, accumulating charge which upon illumination is rapidly dissipated via electron transfer from PSI to the electrode, thereby giving rise to a spike in the current. This in turn suggests that CET and RET pathways which perform light-independent reduction of the PQ pool[7] (Fig. 3a) may influence the Spike Charge feature. CET pathways involve the reduction of the PQ pool with electrons from downstream of PSI, which in cyanobacteria is largely performed by the ferredoxin-dependent NDH-1 complex[77,78]. CET is used to balance the ATP/NADPH ratio of cells to promote carbon fixation, as well as providing protection from photodamage. The thylakoid membrane RET chain of cyanobacteria involves the reduction of the PQ pool by dehydrogenase enzymes, with subsequent oxidation of the pool occurring via terminal oxidase enzymes which use oxygen as a terminal electron acceptor[7].

To test the influence of CET and RET pathways on the Spike Charge, photocurrents were recorded in the presence of DCMU and using 700 nm light to excite PSI selectively, with varying dark adaptation times (the length of the dark period prior to illumination) used to control the extent of light-independent PQ reduction. A clear increase in the Spike Charge was observed at increasing dark adaptation times (Fig. 3b), suggesting the Spike Charge encodes information on the light-independent PQ reduction occurring in the preceding dark period. The same experiments were performed in the presence of electron donors for PQ-reducing dehydrogenase enzymes (Fig. 3a). Addition of NADPH and succinate both provided enhancements in the Spike Charge at all dark adaptation times (Fig. 3ci and Supplementary Fig. 11a-b). This activity can be attributed to the action of NAD(P)H dehydrogenases in the case of NADPH, and to the action of succinate dehydrogenase in the case of succinate[7]. Furthermore, enhancements in the Spike Charge were also observed in thylakoids obtained from mutants lacking all PQH_2-oxidising respiratory terminal oxidase enzymes (Δ*cox*Δ*cyd*Δ*arto*), which have previously been shown to have a more reduced PQ pool caused by lower rates of respiratory oxygen reduction[79,80]. Steady State Photocurrent enhancements were also observed in these conditions with these effects being independent of the dark adaptation time (Fig. 3cii and Supplementary Fig. 11c), demonstrating an enhancement of steady state PSI activity in conditions with a more reduced PQ pool. These results provide a clear demonstration that measurements of the Spike Charge can be used to analyse light-independent PQ reduction performed by CET and RET pathways. Furthermore, photocurrents obtained with thylakoid membranes from species other than *Synechocystis* suggest these PQ-reducing pathways may be specific to cyanobacteria[6,7] (Extended Data Fig. 10 and Supplementary Note 4).

Addition of NADPH and succinate to the electrolyte were also found to provide an enhancement of the dark current (Supplementary Fig. 11d), which could be caused by dehydrogenase enzymes being wired to the electrode- either directly or via $PQ(H_2)$ (Fig. 4a). However, measurements of the dark current could be influenced by abiotic factors, such as changes in capacitance[24]. Direct electron transfer from RET enzymes to the electrode is feasible, as observed in the decay in the Spike Charge magnitude of thylakoid membranes alone at E_{app} values above +200 mV vs SHE (Fig. 2d-e and Extended Data Fig. 6a-b). This phenomenon could be attributed to oxidation of the PQ pool by the electrode in the dark, consistent with cyclic voltammograms of thylakoid membranes exhibiting peaks corresponding to $PQ(H_2)$ (Extended Data Fig. 9), as well as other research demonstrating oxidation of PQH_2 within a lipid bilayer[64]. The decay in Spike Charge magnitude could also be attributed to the respiratory terminal oxidases which are part of the RET chain[7] (Fig. 3a). To test this, E_{app}-dependent changes in the Spike Charge were measured using thylakoid membranes from WT and Δ*cox*Δ*cyd*Δ*arto* cells in the presence of DCMU. Whilst both conditions exhibited a decay in Spike Charge at more positive E_{app} values, this decay was slower in the Δ*cox*Δ*cyd*Δ*arto* mutant, consistent with diminished oxidation of PQH_2 by the electrode (Fig. 3d and Supplementary Fig. 12). Furthermore, the onset of decay was shifted from +200 to +300 mV vs SHE in the mutants. These results can be explained by electron transfer from respiratory terminal oxidases to the electrode at $E_{app} \geq +200$ mV vs SHE, with direct oxidation of PQH_2

occurring at $E_{app} \geq +300$ mV vs SHE (Fig. 4a)- a large overpotential consistent with previous electrochemical measurements performed with synthetic membranes[64].

Spectroelectrochemistry measurements were performed to ensure that these electrochemical measurements of light-independent PQ reduction match those obtained with established spectroscopic methods. A spectroelectrochemical cell was constructed (Supplementary Fig. 4b) for use in a Joliot-type spectrophotometer[30], enabling *in operando* measurements of photocurrents and changes in the oxidation state of the P700 reaction centre of PSI[81] (Fig. 3e-f). The peak of the Spike Charge feature in photocurrent measurements was correlated with the peak of P700 oxidation, further proving the Spike Charge is dependent on PSI electron transfer to the electrode. Addition of NADPH led to an increase in the oxidation of P700 (consistent with it being more reduced prior to illumination due to reduction of the PQ pool by NADPH), with the fold change of the Spike Charge in the presence and absence of NADPH being similar to that of the steady state P700 oxidation (3.3- and 4.6-fold respectively) suggesting the two parameters are equivalent to one another. Furthermore, the rate of P700 re-reduction in the dark was increased in the presence of NADPH by 11-fold, consistent with a faster rate of light-independent P700 reduction via the PQ pool. These results demonstrate that measurements stemming from the thylakoid membrane electrochemistry technique is consistent with established biophysical techniques for analysing thylakoid membrane electron transport, complementing these methods by enabling measurement of electron transfer at multiple points of the electron transport chain.

Discussion

This study develops natural membrane electrochemistry as a method to analyse biological electron transport, presenting a significant advance in bioelectrochemistry research which has largely been limited to studying individual proteins or protein complexes outside of their physiological environment in the absence of their native interaction partners[24]. Whilst pioneering studies have investigated the interactions between natural membranes and electrodes[82–91], they have been limited in their ability to discriminate accurately between different electron transport pathways, thereby hindering analytical applications. Herein we show that with highly structured bio-compatible electrodes, it is possible to perform sensitive measurements of electrochemical parameters which encode information on the functioning of an entire electron transport network. Additionally, mutants, inhibitors and experimental conditions can be leveraged to investigate the catalytic activities of individual enzymes amongst this complex system, without the need for lengthy protein purification.

The results detailed above enable us to construct a model detailing the electron transport pathways occurring within cyanobacterial thylakoid membranes, as well as those occurring between them and the electrode (Fig. 4a). These electron transport pathways are evidenced in multiple experiments (Supplementary Table 1) with DET being the most likely mechanism of interfacial electron transfer (Extended Data Fig. 6 and 9). The results are largely consistent with our understanding of cyanobacterial thylakoid membrane electron transport *in vivo* also[7] (Supplementary Note 5). This model of interfacial electron transfer enables us to use this bioelectrochemical method as an analytical tool for studying thylakoid membrane electron transport activity and its perturbation in different environmental and genetic conditions. This is best demonstrated by the measurements of light-independent PQ reduction in the presence of different electron donors and with different mutant strains (Fig. 3c-d). Thylakoid bioelectrochemistry thereby overcomes the trade-off associated with electrochemical analysis of photosynthetic proteins and cyanobacterial biofilms[50], providing data which is both information-rich and readily interpretable (Fig. 4b). Additionally, thylakoid bioelectrochemistry can be readily coupled to spectroscopic methods commonly used by photosynthesis researchers (Fig. 3e-h), enabling direct measurements of electron transport pathways which are inaccessible to these other techniques.

Given the complexity of the cyanobacterial thylakoid membrane electron transport network[7] (Fig. 1b) we expect that natural membrane electrochemistry could be readily applied to other bioenergetic membranes (Supplementary Note 4 and Extended Data Fig. 10). We foresee that the systems-level understanding of biological electron transport pathways provided by the technique could help bridge the information gap between *in vitro* experiments analysing redox proteins with *in vivo* molecular biology and cell physiology experiments to provide a holistic understanding of bioenergetics. Moving beyond fundamental studies, other apparent applications of natural membrane electrochemistry include the characterisation of drugs and herbicides[92,93] or being used to guide the engineering of electron transport chains for sustainable electricity and chemical production[2].

346 # Methods

347 ## Strains and growth conditions:

348 Cyanobacterial strains (*Synechocystis* sp. PCC 6803 and *Synechococcus elongatus* PCC 7942) were grown
349 photoautotrophically in BG-11 media supplemented with 10 mM bicarbonate[94]. The microalga *Chlamydomonas*
350 *reinhardtii* cw15 (cc-1883) was grown photomixotrophically in TAP medium[95]. Solid cultures used 1.5 % agar
351 (w/v) in the culture medium. Liquid cultures were grown from single colonies cultures under 40 µmol photons
352 m^{-2} s^{-1} at 30 °C, with shaking of 120 rpm and growth tracked by the attenuance at 750 nm (OD_{750}).

353 The plant *Nicotiana benthamiana* was grown under a 16 hr white light (100 µmol photons m^{-2} s^{-1}) / 8 hr dark
354 photoperiod at 21 °C with regular watering. Seeds were stored at 4 °C prior to plantation. Plants were initially
355 germinated from seeds for two weeks, after which seedlings were transferred to individual pots and grown for a
356 further four weeks.

357

358 ## Thylakoid membrane isolation:

359 Cyanobacterial membranes enriched in thylakoids were isolated using a previously described method with
360 numerous modifications[49,57]. One batch provided sufficient sample for ~3 electrodes. Cyanobacterial cultures
361 were grown to mid-stationary phase (OD_{750} = 1.5±0.2), with 50 mL pelleted by centrifugation (3000 x g, 10
362 min) after which the supernatant was removed and discarded. Cell pellets were resuspended in 5 mL of lysis
363 buffer (50 mM 2-(N-Morpholino)ethanesulphonic acid-NaOH (MES-NaOH), 5mM EDTA, 2mM aminocaproic
364 acid, 1mM phenylmethylsulphonyl fluoride, 1X concentration of Roche cOmplete protease inhibitor cocktail,
365 adjusted to pH 6.5) at room temperature and re-centrifuged (3000 x g, 10 min). All subsequent steps were
366 performed at 4 °C away from direct light. The resulting supernatant was removed and discarded, whilst the
367 pellet was resuspended in 900 µL of chilled lysis buffer and transferred to a 2 mL safe-lock microcentrifuge
368 tube. Acid washed glass beads (425-600 µm) were added up to a total volume of 1.75 mL. Cell lysis was
369 performed by two rounds of vortexing on maximum speed for 90 s, followed by a 60 s incubation on ice. The
370 resulting solution was transferred to a 2 mL microcentrifuge tube. The remaining glass beads were washed
371 thrice with 400 µL of lysis buffer (using a 1000 µL pipette tip with the end cut off), with each wash being
372 transferred to the new microcentrifuge tube which was centrifuged to pellet unbroken cells (9000 x g for 1.5
373 min). The supernatant (lysate) was transferred to a 2 mL microcentrifuge tube and centrifuged (15,000 x g for
374 15 min). The supernatant (soluble fraction) was transferred to a brown 15 mL centrifuge tube, with 10 µL being
375 removed and diluted into 990 µL of lysis buffer to determine the C-phycocyanin content. 3 kDa-filtered soluble
376 fraction was prepared by centrifuging through a 3 kDa MWCO Amicon® Ultra-15 Centrifugal Filter Unit
377 (5,000 x g for 1 hour). The remaining pellet (thylakoid membranes) was washed without resuspending in 200
378 µL of lysis buffer and centrifuged (15,000 x g, 15 min). The supernatant was then discarded and the pellet
379 (thylakoid membranes) resuspended in 20 µL of storage buffer (50 mM Tris-HCl, 1M sucrose, adjusted to pH
380 6.5) using a fine paintbrush and transferred to a dark. This thylakoid membrane suspension was transferred to a
381 brown 500 µL microcentrifuge tube, with 1 µL being removed and diluted into 999 µL of methanol to determine
382 the chl *a* concentration. The thylakoid membrane suspension was then diluted with storage buffer to a final chl *a*
383 concentration of 2 µg $µL^{-1}$, unless otherwise stated.

384 Green algal thylakoid membranes were isolated from 150 mL of *C. reinhardtii* culture grown to mid-
385 exponential phase (OD_{750}=0.9±0.05) using a previously developed extraction method[96]. One batch prepared
386 according to this method provided sufficient thylakoid membranes for ~3 electrodes. Following extraction, 1 µL
387 of thylakoid membrane suspension was diluted in 999 µL of a 4:1 acetone to methanol mixture to determine the
388 chl *a*+*b* concentration. The thylakoid membrane suspension was then diluted to a final chl *a*+*b* concentration of
389 750 ng $µL^{-1}$.

390 Plant thylakoid membranes were isolated from 4 g of *N. benthamiana* leaves using extraction method A2 from
391 Chen *et al*[97]. One batch prepared according to this method provided sufficient thylakoid membranes for ~20
392 electrodes. Following extraction, 1 µL of thylakoid membrane suspension was diluted in 999 µL of a 4:1
393 acetone to methanol mixture to determine the chl *a*+*b* concentration. The thylakoid membrane suspension was
394 then diluted to a final chl *a*+*b* concentration of 4 µg $µL^{-1}$.

395

396 ## Electrode preparation:

IO-ITO electrodes for electrochemistry experiments were made according to a previously developed protocol with modifications[48]. Fluorine-doped tin oxide-coated glass (Merck, 735167, 7 Ω sq^{-1}) cut into 1 cm x 3 cm rectangles was used as a support. These were first cleaned by bath sonication in isopropanol and then in ethanol. After drying in an oven at 100 °C for 1 hr, circular stencils of 1 cm diameter were made on the conductive face with electrical tape. The slides were UV-ozone treated using a Bioforce Nanosciences UV-Ozone Procleaner for 15 min. 1 mL of a 2.5% (w/w) solution of polystyrene beads (AlfaAesar, 42717, 10 µm) was centrifuged (15,000 x g, 4 min), with 750 µL of the supernatant being discarded. The pellet was then resuspended in the remaining supernatant, with 30 µL of the resulting solution being dropcast into the circular stencils and spread evenly. The electrodes were left at room temperature for 2 hr in a covered glass Petri dish to allow for polystyrene beads to settle and dry. Following this, annealing was performed at 80 °C for 10 min. Meanwhile, 80 mg of ITO nanoparticles (Merck, 544876, <50 nm) were bath sonicated at 37 kHz in 300 µL 5:1 methanol:Milli-Q® for 6 hr. 7.5 µL of the suspension was drop cast evenly onto the polystyrene scaffold and left until it had fully infiltrated the structure. Electrodes were then heated in a Carbolite ELF 11/14B/301 furnace at 500 °C for 20 min from room temperature with a temperature ramp of 1 °C min^{-1} to calcinate the polystyrene beads.

IO-ITO electrodes for spectroelectrochemistry were made by the same protocol with the following modifications. ITO-coated glass (Diamond Coatings, 4.5 Ω sq^{-1}) cut into 0.5 cm x 6 cm rectangles was used as a support. 10 µL of a 10% (w/w) solution of polystyrene beads (Merck, 72986, 10 µm) was dropcast into the circular stencils and spread evenly. Electrodes were left at 4 °C overnight followed by 1 hr at room temperature to settle and dry. Annealing was performed at 100 °C for 10 min. 1 µL of ITO nanoparticle suspension was drop cast on the polystyrene scaffold.

Electron microscopy:

Electron microscopy was performed with a TESCAN MIRA3 FEG-SEM with beam acceleration of 30 kV.

Scanning electron microscopy of electrodes was performed. Where necessary, samples were left to dry at 4 °C overnight. Prior to imaging, samples were sputter coated with a 10 nm Pt layer using a Quorum Technologies Q150T ES Turbo-Pumped Sputter Coater.

Scanning transmission electron microscopy of isolated thylakoids membranes was performed. Samples were diluted to a chl *a* concentration of 1 ng μL^{-1} in deionised water. 2 µL of this solution was pipetted onto a holey carbon-supported copper TEM grid (200 mesh) and left to dry at 4 °C for 2 hr prior to imaging.

Thylakoid membrane electrochemistry:

Electrode modification

Thylakoid membrane modification of electrodes was performed by drop casting thylakoid membrane suspension over the structured area of the electrode in a circular motion (10 µL for photoelectrochemistry and 3.7 µL for spectroelectrochemistry), with care taken to spread the solution evenly across the electrode structure. Electrodes were then left to dry for ~20 min at room temperature, after which they had a glazed (as opposed to wet or cracked) appearance and were used in electrochemistry experiments.

Photoelectrochemistry

Photoelectrochemistry of thylakoid membranes was performed in a water-jacketed, glass photoelectrochemical cell with a PTFE lid, maintained at 25 °C and containing 4.5 mL of electrolyte. Measurements were performed with an Ivium Technologies CompactStat.h potentiostat using a thylakoid membrane-modified IO-ITO working electrode, platinum mesh counter electrode and Ag/AgCl reference electrode. Illumination was provided with Thorlabs LED light sources (M680L4, M700L4, M730L5) powered by an LED driver) and aligned with a collimator. An additional FB730-10 - Ø1" Bandpass Filter filter (2.54 mm, Thorlabs) was used with the 730 nm LED.

Spectroelectrochemistry

Spectroelectrochemistry of thylakoid membranes was performed in a photoelectrochemical cell made from a 4 mL quartz crystal cuvette with a PTFE lid, maintained at room temperature and containing 2.4 mL of electrolyte. Measurements were performed with an Ivium pocketSTAT2 potentiostat using a platinum mesh

counter electrode and platinum pseudoreference. E_{app} values were calibrated by performing cyclic voltammetry of 500 µM ferricyanide and 500 µM ferrocyanide with a glassy carbon working electrode and comparing the measured E_m with those measured in a glass vial using the same working and counter electrode with a Ag/AgCl reference electrode. Measurements were performed alongside spectroscopic measurements within a JTS-150, which also provided illumination from the 630 nm actinic light ring. These measurements were otherwise performed identically to standard photoelectrochemistry experiments.

Standard Conditions

Unless otherwise stated, all measurements were performed in following standard conditions: chl *a* loading, 20 µg; illumination, 50 µmol photons m^{-2} s^{-1} of chopped 680 nm light; electrolyte, electrolyte buffer (50 mM MES-NaOH, 15 mM NaCl, 5 mM $MgCl_2$, 2 mM $CaCl_2$, adjusted to pH 6); sampling rate, 10 s^{-1}; purging, N_2 gas for 20 min before and 5 min after addition of the working electrode with the purging needle moved to the headspace during measurement. Chronoamperometry scans were performed with chopped light (1 min light / 1 min dark) and an applied working electrode potential (E_{app}) of +300 mV vs SHE following 5 min pre-equilibration, unless otherwise stated. When possible, three successive photocurrent measurements were performed and average (see below). Stepped chronoamperometry scans were recorded with chopped light (90 s dark / 30 s light / 30 s dark) for measurements at each E_{app} value which ranged -100 to +700 mV vs SHE without, or -600 to +700 mV with, enzymatic oxygen removal provided by 5 mM glucose (Merck, G8270), 1 mg mL^{-1} glucose oxidase (Merck, G7141), and 500 µg mL^{-1} catalase (Merck, C9322)[70]. Measurements were performed following 10 min of pre-equilibration, with two measurements of the first E_{app} value being recorded with only the latter being used in data analysis.

Other experimental conditions

Some experiments were performed in non-standard conditions. These include the use of different light conditions (intensity, wavelength or chopping), no purging, different pH, or differently electrolytes such as electrolyte buffer - salts (50 mM MES-NaOH, adjusted to pH 6) and phosphate buffer (43.2 mM NaH_2PO_4, 6.8 mM Na_2HPO_4, adjusted to pH 6). For some experiments the electrolyte was supplemented with different concentrations of the following chemicals: Carbonyl cyanide m-chlorophenyl hydrazone (CCCP; Merck, C2759; stock, 100 mM in DMSO), 3-(3,4-dichlorophenyl)-1,1-dimethylurea (DCMU; Merck, D2425; working, 100 µM; stock, 100 mM in DMSO), N-oxo-2-heptyl-4-Hydroxyquinoline (HQNO; Cayman Chemical, 15159; working, 10 µM; stock, 1 mM in DMSO), potassium ferricyanide (Merck, 244023; working, 1 mM; stock, 500 mM in electrolyte buffer), $NADP^+$ (Cayman Chemical, 21045; working, 1 mM; stock, 50 mM in electrolyte buffer), NADPH (Merck, 481973; working, 1 mM; stock, 50 mM in electrolyte buffer), PMA (Merck, P27127; stock, 50 mM in DMSO), soluble fraction (working, 160 ng μL^{-1} prior to any filtration), succinate (Merck, 14160; working 5 mM; stock, 1M in electrolyte buffer). Chemical titrations were performed by successively adding chemical stocks to the electrolyte between measurements. The electrolyte was mixed with a 5000 µL pipette, with 5 min of purging prior to each measurement. pH titrations were performed from high to low pH by replacing the electrolyte with a new solution adjusted to the desired pH with HCl and NaOH, with 20 min of purging prior to each measurement. Photocurrent measurements with different light intensities were performed by increasing the power of the LED in the dark period between photocurrent measurements. Photocurrent measurements with different dark adaptation times were changing the programmed light chopping in the dark period between photocurrent measurements.

Photocurrent data analysis:

Analysis and plotting of thylakoid membrane photocurrents were performed in bespoke software developed in MATLAB. The software accepts raw data files as inputs, alongside various experimental and other parameters. An option is included to normalise the data by chl content (in nmol), which is provided by the user. Analysis of chronoamperometry and stepped chronoamperometry data was performed by processing the data from individual photocurrent measurements in steps depicted in Extended Data Fig. 4b, with example code provided (Supplementary Code).

Dark current measurement

Dark currents were calculated from raw photocurrent data as follows:

$$I_{dc}\ (\mathrm{A}) = \frac{\sum_{t=t_{\mathrm{deq}}}^{t_{\mathrm{end}}} I_{\mathrm{exp}}(t)}{t_{\mathrm{end}} - t_{\mathrm{deq}}}$$

where I_{dc} is the dark current, $I_{\text{exp}}(t)$ is the experimental current data at time t, t_{deq} is the dark equilibration time (time at which the dark current reaches steady state) and t_{end} is the final timepoint of the data.

Baselining

Baselining was performed by fitting to the dark signal. Fitting was performed with a straight line for most data. For electrochemical data in which a straight line provided a poor fit (especially true of stepped chronoamperometry data), dark current was fitted with the following treatment of the Cottrell equation for a spherical electrode[98]:

$$I_{\text{fit}}\left(t \mid 0 \leq t < t_{on} \cup t_{\text{deq}} < t \leq t_{end}\right) \text{ (A)} = nFA\left(\frac{\sqrt{Dc_0}}{\sqrt{\pi t}} + \frac{Dc_0}{r}\right)$$

where $I_{\text{fit}}(t)$ is the fitted current at time t, t_{on} is the time at the start of the light period, t_{deq} is the dark equilibration time (time at which the dark current reaches steady state), t_{end} is the final timepoint of the data, n is the number of electrons involved in the redox reaction of the analyte, F is Faraday's constant, A is the planar surface area of the electrode, D is the diffusion coefficient of the analyte, c_0 is the concentration of analyte at $t = 0$, and r is the radius of the electrode. All parameters were fitted apart from r, which was set as 5 mm. Fitting was performed using the fminsearch function to minimise the sum of squared estimate of errors (SSE) between the data and the fit, as follow:

$$SSE = \sum_{t=0}^{t_{\text{end}}} \left[I_{\text{exp}}(t) - I_{\text{fit}}(t)\right]$$

where $I_{\text{exp}}(t)$ and $I_{\text{fit}}(t)$ are the experimental and fitted current at time t, and t_{end} is the final timepoint of the data. Because the position of $t = 0$ is not known, curve fitting is performed at increasing values of the parameter until an optimal fit is identified.

In stepped chronoamperometry experiments the dark current was found to be offset between different replicates, likely caused by differences in electrode capacitance at more positive E_{app} values. To account for this, dark currents were shifted to an average value prior to baselining, as follows:

$$I_{\text{adj}}(n,t) \text{ (A)} = I_{\text{exp}}(n,t) - \left(I_{\text{exp}}(n,t_{\text{end}}) - \frac{\sum_1^N I_{\text{exp}}(n,t_{\text{end}})}{N}\right)$$

where $I_{\text{exp}}(n,t)$ $I_{adj}(n,t)$ are the experimental and adjusted experimental current for replicate n at time t, t_{end} is the final timepoint of the data, and N is the total number of replicates.

Final fitted curves were subtracted from experimental data to provide baselined photocurrent data:

$$I_{\text{base}}(t) \text{ (A)} = I_{\text{exp}}(t) - I_{\text{fit}}(t)$$

where $I_{\text{exp}}(t)$ and $I_{\text{base}}(t)$ are the experimental and baselined current at time t.

Photocurrent parameter measurements

Steady State Photocurrents were calculated from baselined photocurrents as follows:

$$I_{ssp} \text{ (A)} = \frac{\sum_{t=t_{\text{leq}}}^{t_{\text{off}}} I_{\text{base}}(t)}{t_{\text{off}} - t_{\text{leq}}}$$

where I_{ssp} is the Steady State Photocurrent, t_{off} is the time at the end of the light period and t_{leq} is the light equilibration time (time at which the light current reaches steady state), and $I_{\text{base}}(t)$ is the baselined current at time t .

Spike Charges were calculated from baselined photocurrents using the trapz function as follows:

$$Q_{sc} \text{ (C)} = \int_{t_{\text{on}}}^{t_{\text{off}}} \left[I_{base}(t) - I_{ssp}\right] dt$$

where Q_{sc} is the Spike Charge, t_{on} and t_{off} are the times at the start and end of the light period, $I_{\text{base}}(t)$ is the baselined current at time t, and I_{ssp} is the Steady State Photocurrent.

Averaging replicates

For chronoamperometry data, three successive photocurrents were recorded for each tested condition. The mean of these photocurrents and their respective parameters were calculated to reduce noise. For all photocurrent measurements, the mean and standard error of the mean (S.E.M.) were calculated for photocurrents and their parameters from three independent biological replicates.

Nanoparticle tracking analysis:

Nanoparticle tracking analysis (NTA) was performed using a Malvern Panalytical Nanosight NS500 fitted with an Electron Multiplying Charge Coupled Device camera configured with a 522 nm laser. Particle concentrations were determined by tracking and counting particles in microscopy images. Particle sizes were determined based on the diffusion speed of tracked particles. Thylakoid membrane samples were diluted to a chl *a* concentration of 10 pg μL^{-1} in electrolyte buffer, with 5 x 60 s videos recorded for each sample and analysed with NTA 3.2 software using a detection threshold of 5.

Membrane topology analysis:

The polarity of cyanobacteria TMs was determined by 2-phase polymer partitioning[58]. All steps were performed at 4 °C. Solutions of dextran-500 (11.6% w/w) and PEG-3350 (11.6% w/w) were prepared in partitioning buffer (5 mM K2HPO4, 250 mM sucrose, adjusted to pH 7.8 with HCl or NaOH). 20 µg of isolated thylakoid membranes were deposited into a 2 mL microcentrifuge tube containing 750 µL of PEG-3350 solution layered on top of 750 µL of dextran-500 solution. Tubes were mixed by inverting 35 times before phase partitioning by centrifugation (1000 x g, 4 min). The upper phase was added to a fresh 2 mL microcentrifuge tube containing 750 µL of dextran-500 partitioning buffer. The lower phase was topped with 750 µL of fresh PEG-3350 partitioning buffer. Mixing and phase partitioning was subsequently repeated twice, after which the upper and lower phases from all tubes were pooled into separate 15 mL centrifuge tubes and subjected to one final phase partitioning. The upper and lower phases from each tube were again pooled in 50 mL centrifuge tubes, diluted up to 30 mL with partitioning buffer, and centrifuged (50,000 x g, 15 min) to pellet the thylakoid membranes. Supernatants were discarded, with pellets being resuspended in 1 mL of methanol and transferred to 1.5 mL microcentrifuge tubes. Centrifugation (13,000 x g, 3 min) was used to remove debris, after which the chl *a* concentration of the supernatants were determined. The proportion of thylakoids which were cytoplasmic side-out was determined as follows:

$$\text{Cytoplasmic side–out} = \frac{[\text{Chl a}]_{\text{lower phase}}}{[\text{Chl a}]_{\text{lower phase}} + [\text{Chl a}]_{\text{upper phase}}}$$

Fluorimetry:

Excitation-emission matrices were recorded with an Agilent Cary Eclipse Fluorescence Spectrometer. Measurements were performed with excitation and emission wavelengths ranging from 200-800 nm, using a step size of 5 nm, scan rate of 1000 nm min^{-1}, averaging time of 0.3 s, excitation and emission bandwidths of 5 nm, and a PMT detector sensitivity of 500 V. For measurements of isolated thylakoid membranes, a chl *a* concentration of 10 ng μL^{-1} was used. For measurements of soluble fractions, a (pre-filtration) C-phycocyanin concentration of 160 ng mL^{-1} was used.

Pigment quantification:

UV-visible spectroscopy was performed using a Shimadzu UV-1800 Spectrophotometer. Absorbance spectra were recorded in plastic 1 mL cuvettes from 350 to 800 nm using a suitable blank.

Chl *a* concentrations of cyanobacterial cultures were calculated as follows[80]:

$$[\text{Chl } a]\ (\mu\text{g}\ \mu\text{L}^{-1}) = \frac{\text{OD}_{680} - \text{OD}_{750}}{103.1}$$

581 Chl *a* concentrations of cyanobacterial thylakoid membrane samples were determined in methanol as follows[99]:

582 $$[\text{Chl } a]\ (\mu\text{g}\ \mu\text{L}^{-1}) = \frac{\text{OD}_{665} - \text{OD}_{750}}{79.95}$$

583 Chl *a* and *b* concentrations of algal and plant thylakoid membrane were determined in a 4:1 acetone to methanol
584 mixture as follows[99]:

585 $$[\text{Chl } a + b]\ (\mu\text{g}\ \mu\text{L}^{-1}) = \frac{17.76(\text{OD}_{647} - \text{OD}_{750}) + 7.34(\text{OD}_{664} - \text{OD}_{750})}{1000}$$

586 The C-phycocyanin concentration of the soluble fraction diluted in lysis buffer was determined as follows[100]:

587 $$[\text{C-phycocyanin}]\ (\mu\text{g}\ \mu\text{L}^{-1}) = \frac{\text{OD}_{620} - (0.7 \times \text{OD}_{750})}{7.38}$$

588

589 **SDS-PAGE:**

590 SDS-PAGE was performed with cyanobacterial lysate, soluble fraction, and isolated thylakoid membranes.
591 Total protein concentrations of each sample were determined by a Bradford assay[101] against a standard curve
592 obtained with 0, 10, 50, 250, 500 and 1000 µg mL^{-1} Bovine Serum Albumin (Merck, A2153), with 30 µg of
593 protein in each lane. Samples were mixed with an appropriate volume of 4X Laemmli buffer in PCR tubes and
594 heated to 100 °C for 10 min. Samples were then centrifuged (13,000 x g, 5 min) with the resulting supernatant
595 loaded onto a BioRad Mini-PROTEAN® TGX® Stain-Free Gel (4-20%). 7 µL of PageRuler™ Plus Prestained
596 Protein Ladder (10 to 250 kDa) was used. Gels were run for 75 min at 100 V in SDS running buffer (25.01 mM
597 Tris base, 192.4 mM glycine, 3.467 mM SDS).

598

599 **Oxygen evolution measurements:**

600 Oxygen evolution measurements were recorded with a Pyroscience FireSting®-PRO using a OXROB10-HS
601 High Speed Robust Oxygen Probe inserted into 1 mL of solution within a 5 mL glass vial. Thylakoid membrane
602 suspensions were prepared by diluting isolated thylakoid membranes in electrolyte buffer (pH 6). Cell solutions
603 were prepared by concentrating cells in BG-11 medium (pH 7.8). Measurements were performed at 25 °C with
604 stirring at 900 rpm. PSII oxygen evolution measurements were performed with a chl *a* concentration of 40 µg
605 mL^{-1} in the presence of 1 mM DCBQ (Merck, 431982) and 1 mM potassium ferricyanide as electron
606 acceptors[49]. PSI oxygen evolution measurements were performed with a chl *a* concentration of 20 µg mL^{-1} in the
607 presence of 100 µM DCMU, 20 mM ascorbate (Merck, 11140) and 200 µM DCPIP (Merck, D1878) as electron
608 donors, with 4 mM methyl viologen (Merck, 856177) as an electron acceptor[102]. Samples were left to pre-
609 equilibrate to a steady O_2 level prior to measurement under 1500 µmol photons m^{-2} s^{-1} of chopped 680 nm (2
610 min light, 2 min dark). Data was baselined to the pre-equilibration signal and subsequently analysed by
611 independently fitting the light and dark currents to the following equation:

612 $$[\text{O}_2]\ (\mu\text{mol L}^{-1}) = (k_{O_2} \times t) + \text{c}$$

613 where k_{O_2} is the O_2 production rate (µmol s^{-1}), t is time (s) from beginning of the light/dark period and c is the
614 [O_2] at t=0. The electron transfer rate, measured as the absolute oxygen evolution rate, was calculated as
615 follows:

616 $$\text{Electron Transfer Rate } (\Delta\text{nmol O}_2\ [\text{nmol chl a}]^{-1}\ \text{hr}^{-1}) = \left|\frac{3600\left(k_{O_2}^{light} - k_{O_2}^{dark}\right)}{\text{Chl a}}\right|$$

617 where $k_{O_2}^{light}$ and $k_{O_2}^{dark}$ are the O_2 production rates (µmol s^{-1}) in the light and dark, with the mass of Chl *a*
618 expressed in nmol.

619

620 **Spectroscopic measurements of thylakoid membranes:**

621 Biophysical measurements of thylakoid membranes were performed using a BioLogic JTS-150 Spectrometer.
622 Measurements were performed at room temperature in 4 mL crystal quartz cuvettes containing 2 mL of

electrolyte buffer supplemented with cyanobacterial thylakoid membranes to a final chl *a* concentration of 10 µg mL^{-1}.

Chlorophyll fluorescence

Chl fluorescence measurements were performed under increasing intensities of chopped 630 nm light (1 min light / 1 min dark) using 1 mM potassium ferricyanide as an electron acceptor. A 450 nm measuring light was used as an excitation beam, with a 700 nm High Performance long-pass filter (5 mm, Edmund Optics) on the measuring detector and a BG39 filter (3 mm, Schott) on the reference detector. A detector current of 50 mA was used with 150 µs detecting pulses recorded within a 1 ms dark interval. The sample was further excited with a 99 ms multiple turnover flash of 7000 µmol m^{-2} s^{-1} at 40 s into the light and dark period. PSII quantum efficiency was calculated as follows[29]:

$$\Phi_{\mathrm{PSII}} = \frac{F'_{\mathrm{m}} - F_{\mathrm{m}}}{F'_{\mathrm{m}}}$$

where Φ_{PSII} is the PSII quantum efficiency, and F_{m} and F'_{m} are the maximum fluorescence in the dark and light respectively.

Redox cofactor absorbance

Cytochrome *b* and *f* redox changes were recorded under increasing intensities of chopped 630 nm light (1 min light / 1 min dark) using 1 mM potassium ferricyanide as an electron acceptor. 546, 554, 563 and 574 nm measuring lights were used, with BG39 filters (3 mm, Schott) on the measuring and reference detectors. A detector voltage of 5V was used with 150 µs detecting pulses recorded within a 1 ms dark interval. The amount of oxidised cytochrome *b* and *f* were calculated as follows[37]:

$$[\mathrm{Cyt}\ b_{\mathrm{ox}}]_{\mathrm{exp}}(t)\ \left(\frac{\Delta \mathrm{I}}{\mathrm{I}}\right) = A_{563}(t) - (0.607A_{574}(t) + 0.393A_{546}(t))$$

$$[\mathrm{Cyt}\ f_{\mathrm{ox}}]_{\mathrm{exp}}(t)\ \left(\frac{\Delta \mathrm{I}}{\mathrm{I}}\right) = A_{554}(t) - (0.607A_{574}(t) + 0.393A_{546}(t))$$

where $[\mathrm{X}_{\mathrm{ox}}](t)$ is the experimental amount of oxidised cofactor and $A_x(t)$ is the absorbance change recorded at wavelength x and time t.

Plastocyanin and P700 redox changes were recorded under increasing intensities of chopped 630 nm light (1 min light / 1 min dark) using 1 mM methyl viologen as an electron acceptor. 705 and 740 nm measuring lights were used, with RG695 filters (3 mm, Schott) on the measuring and reference detectors. A detector voltage of 4V was used with 100 µs detecting pulses recorded within a 1 ms dark interval. The amount of oxidised plastocyanin and P700 were calculated as follows[81]:

$$[\mathrm{Plastocyanin}_{\mathrm{ox}}]_{\mathrm{exp}}(t)\ \left(\frac{\Delta \mathrm{I}}{\mathrm{I}}\right) = A_{740}(t)$$

$$[\mathrm{P700}^{+}]_{\mathrm{exp}}(t)\left(\frac{\Delta \mathrm{I}}{\mathrm{I}}\right) = A_{705}(t) - A_{740}(t)$$

where $[\mathrm{X}](t)$ is the experimental amount of oxidised cofactor and $A_x(t)$ is the absorbance change recorded at wavelength x and time t.

Photoresponses were baselined to the dark signal (see above). Steady state redox changes of cofactors were calculated from baselined redox changes as follows:

$$[\mathrm{X}]_{ss}\ \left(\frac{\Delta \mathrm{I}}{\mathrm{I}}\right) = \left|\frac{\sum_{t=t_{\mathrm{leq}}}^{t_{\mathrm{off}}} [\mathrm{X}]_{\mathrm{base}}(t)}{t_{\mathrm{off}} - t_{\mathrm{leq}}}\right|$$

where $[X]_{ss}$ is the steady state redox change of cofactor X, t_{leq} is the light equilibration time (time at which the light current reaches steady state), t_{off} is the time at the end of the light period, and $[\mathrm{X}]_{\mathrm{base}}$ is the baselined amount of oxidised cofactor at time t. The absolute value of this parameter corresponds to the oxidation of P700 and cytochromes *b* and *f*, and the reduction of plastocyanin.

The rate of P700 re-reduction in the dark was calculated by fitting the following exponential decay curve to the first 7 seconds of the dark signal[103]:

$$[\mathrm{P700}^+]_{\mathrm{base}}(t \mid t_{\mathrm{off}} \leq t < t_{\mathrm{off}} + 7)\left(\frac{\Delta \mathrm{I}}{\mathrm{I}}\right) = Be^{-t/\tau} + [\mathrm{P700}^+]_{\mathrm{base}}(t_{\mathrm{off}})$$

where $[\mathrm{P700}^+]_{\mathrm{base}}(t)$ is the baselined amount of oxidised P700, t_{off} is the time at the end of the light period, B is a scaling factor, and τ is the time constant. The rate of P700 re-reduction was subsequently calculated as the inverse of τ.

NADPH fluorescence

NADPH fluorescence measurements were performed under 500 µmol m^{-2} s^{-1} of chopped 630 nm light (1 min light / 10 min dark) using 1 mM $NADP^+$ as an electron acceptor. A 385 nm measuring light was used as an excitation beam, with a BG39 filter (3 mm, Schott) and a custom 500 nm long-pass filter on the measuring detector, with a BG39 filter (3 mm, Schott) on the reference detector[104]. A detector current of 100 mA was used with 100 µs detecting pulses recorded within a 1 ms dark interval. Photoresponses were baselined to the dark signal (see above).

Electrochromic shift

Electrochromic shift measurements were performed under 500 µmol photons m^{-2} s^{-1} of 630 nm light (1 min light / 1 min dark) using 1 mM potassium ferricyanide as an electron acceptor. 480 and 500 nm measuring lights were used[19,105], with BG39 filters (3 mm, Schott) on the measuring and reference detectors. A detector voltage of 5 V was used with 100 µs detecting pulses, recorded within a 200 µs dark interval for the final 10 s of the light period and first 10 s of the dark period, or within a 1 ms dark interval otherwise. Photoresponses were baselined to the dark signal (see above).

Quantum crystal microbalance with dissipation:

Quartz Crystal Microbalance with Dissipation (QCM-D) was performed using a Biolin Scientific QSense E4 QCM with gold sensors (Biolin Scientific, QSX 301) sputter coated with a 10 nm layer of ITO using a Quorum Technologies Q150T ES Turbo-Pumped Sputter Coater. Sensors were cleaned prior to use by being submerged in 1% Hellmanex II for 30 min, rinsed with ultrapure water, and dried with N_2 gas. Sensors were then sonicated in 99% ethanol for 10 min, rinsed with ultrapure water, dried with N_2 gas, and UV-ozone treated for 10 min using a Bioforce Nanosciences UV-Ozone Procleaner. A flow rate of 150 µL min^{-1} was used for all experiments. After each solution was pumped into the flow cell the pumping was stopped. The sensors were left until no observable changes in frequency or dissipation were observed before further solutions were pumped in. Sensors were pre-equilibrated in electrolyte buffer for 1 hr before measurements. Thylakoid membrane suspensions were diluted to a chl *a* concentration of 100 ng μL^{-1} in storage buffer prior to being pumped into the flow cell.

Protein structure analysis:

Structure of photosynthetic complexes were visualised with UCSF ChimeraX[106]. Models of PSII dimers (isolated from *Thermostichus vulcanus*, PDB: 3WU2[107]), cytochrome b6f dimers (isolated from *Nostoc* sp. PCC 7120, PDB: 4H44[108]), and PSI trimers (isolated from *Thermosynechococcus vestitus* BP-1, PDB: 1JB0[109]) embedded within simulated lipid bilayers were obtained from the MemProtMD database[63]. Ligands were added to models by alignment with the biological assemblies obtained from the PDB database. In the case of PSI, molecular dynamics simulations had only been performed on the protein monomer, despite the biological assembly being a trimer. A lipid bilayer model for the trimer was made by aligning the MemProtMD structure with each of the monomer chains, followed by the deletion of any clashing lipid residues (van der Waals overlap ≥ 0.6 Å after subtracting 0.4 Å for hydrogen bonding).

Cyclic voltammetry:

All cyclic voltammetry experiments were performed with an Ivium Technologies CompactStat.h following 20 minutes of purging with N2 gas, with the purging needle being moved to the headspace of the electrochemical cell during measurement.

Cyclic voltammetry of lysis buffer, soluble fractions and the ferri-/ferrocyanide redox couple (500 µM ferricyanide and 500 µM ferrocyanide) was performed in a 20 mL glass filled with 5 mL of solution, using an ITO-coated glass working electrode, platinum mesh counter electrode, and Ag/AgCl reference electrode. Measurements were performed following a 1 min pre-equilibration at -600 mV vs SHE, after which E_{app} was changed from -600 to +700 mV vs SHE with a scan rate of 10 mV s^{-1}. The third and final scan was plotted. Soluble fractions were not diluted prior to measurement.

All other cyclic voltammetry experiments were performed with the same electrochemical apparatus used in thylakoid membrane photoelectrochemistry experiments. Measurements were performed following a 5 min pre-equilibration at +800 mV vs SHE, after which E_{app} was changed from +800 to -200 mV vs SHE with a scan rate of 2 mV s^{-1}. The first and only scan was plotted. Measurements of different electrolytes and redox molecules were performed with blank IO-ITO electrodes. Measurements of redox molecules were performed in electrolyte buffer with the following concentrations: 10 µM HQNO, 1 mM ferri-/ferrocyanide redox couple (500 µM ferricyanide and 500 µM ferrocyanide), 500 µM $NADP^+$ and 500 µM NADPH. Measurements of thylakoid membrane-modified IO-ITO electrodes were performed in darkness or under 50 µmol photons m^{-2} s^{-1} of 680 nm in the presence of either 1% DMSO, 100 µM DCMU or 10 µM HQNO.

The position of redox peaks was determined using the "findpeaks" function in MATLAB when possible, with other clearly visible peaks being annotated manually. E_m values were calculated as the midpoint between a pair of oxidation and reduction peaks.

Data Availability

All raw data is available at https://github.com/JLawrence96/Dissecting-a-biological-electron-transport-network-with-electrochemistry.git.

Code Availability

All code is available at https://github.com/JLawrence96/Dissecting-a-biological-electron-transport-network-with-electrochemistry.git.

References

1. Nicholls, D. G. & Ferguson, S. J. *Bionergetics 4th Edition*. (Academic Press, Cambridge, Massachusetts, 2013).

2. Lawrence, J. M. *et al.* Rewiring photosynthetic electron transport chains for solar energy conversion. *Nat. Rev. Bioeng.* **1**, 887–905 (2023).

3. Atkinson, J. T., Chavez, M. S., Niman, C. M. & El-Naggar, M. Y. Living electronics: A catalogue of engineered living electronic components. *Microb. Biotechnol.* **16**, 507–533 (2023).

4. Peters, J. W. *et al.* A new era for electron bifurcation. *Curr. Opin. Chem. Biol.* **47**, 32–38 (2018).

5. Kaila, V. R. I. & Wikström, M. Architecture of bacterial respiratory chains. *Nat. Rev. Microbiol.* **19**, 319–330 (2021).

6. Blankenship, R. E. *Molecular Mechanisms of Photosynthesis*. (Wiley, 2021).

7. Lea-Smith, D. J., Bombelli, P., Vasudevan, R. & Howe, C. J. Photosynthetic, respiratory and extracellular electron transport pathways in cyanobacteria. *Biochim. Biophys. Acta Bioenerg.* **1857**, 247–255 (2016).

8. Goldman, A. D., Weber, J. M., LaRowe, D. E. & Barge, L. M. Electron transport chains as a window into the earliest stages of evolution. *Proc. Natl. Acad. Sci. U.S.A.* **120**, e2210924120 (2023).

9. Spinelli, J. B. *et al.* Fumarate is a terminal electron acceptor in the mammalian electron transport chain. *Science* **374**, 1227–1237 (2021).

10. Valeros, J. *et al.* Rhodoquinone carries electrons in the mammalian electron transport chain. *Cell* **188**, 1084–1099 (2025).

11. Gawryluk, R. M. R. & Stairs, C. W. Diversity of electron transport chains in anaerobic protists. *Biochim. Biophys. Acta Bioenerg.* **1862**, 148334 (2021).

12. Unden, G. & Bongaerts, J. Alternative respiratory pathways of Escherichia coli: energetics and transcriptional regulation in response to electron acceptors. *Biochim. Biophys. Acta Bioenerg.* **1320**, 217–234 (1997).

13. Sturm, G. *et al.* A dynamic periplasmic electron transfer network enables respiratory flexibility beyond a thermodynamic regulatory regime. *ISME J.* **9**, 1802–1811 (2015).

14. Robb, E. L. *et al.* Control of mitochondrial superoxide production by reverse electron transport at complex I. *J. Biol. Chem.* **293**, 9869–9879 (2018).

15. Bennett, C. F., Latorre-Muro, P. & Puigserver, P. Mechanisms of mitochondrial respiratory adaptation. *Nat. Rev. Mol. Cell. Biol.* **23**, 817–835 (2022).

16. Liu, L. N. *et al.* Control of electron transport routes through redox-regulated redistribution of respiratory complexes. *Proc. Natl. Acad. Sci. U.S.A.* **109**, 11431–11436 (2012).

17. Hanke, G. T., Endo, T., Satoh, F. & Hase, T. Altered photosynthetic electron channelling into cyclic electron flow and nitrite assimilation in a mutant of ferredoxin:NADP(H) reductase. *Plant Cell Environ.* **31**, 1017–1028 (2008).

18. Kramer, M. *et al.* Regulation of photosynthetic electron flow on dark to light transition by ferredoxin:NADP(H) oxidoreductase interactions. *eLife* **10**, e56088 (2021).

19. Nikkanen, L. *et al.* Functional redundancy between flavodiiron proteins and NDH-1 in Synechocystis sp. PCC 6803. *Plant J.* **103**, 1460–1476 (2020).

20. Foyer, C. H. & Hanke, G. ROS production and signalling in chloroplasts: cornerstones and evolving concepts. *Plant J.* **111**, 642–661 (2022).

21. Krieger-Liszkay, A. & Shimakawa, G. Regulation of the generation of reactive oxygen species during photosynthetic electron transport. *Biochem. Soc. Trans.* **50**, 1025–1034 (2022).

22. Vercellino, I. & Sazanov, L. A. The assembly, regulation and function of the mitochondrial respiratory chain. *Nat. Rev. Mol. Cell. Biol.* **23**, 141–161 (2021).

23. Monti, D., Ottolina, G., Carrea, G. & Riva, S. Redox reactions catalyzed by isolated enzymes. *Chem. Rev.* **111**, 4111–4140 (2011).

24. Butt, J. N., Jeuken, L. J. C., Zhang, H., Burton, J. A. J. & Sutton-Cook, A. L. Protein film electrochemistry. *Nat. Rev. Methods Primers* **3**, 1–19 (2023).

25. Richardson, K. H. *et al.* Functional basis of electron transport within photosynthetic complex I. *Nat. Commun.* **12**, 1–8 (2021).

26. Verkhovskaya, M. L., Belevich, N., Euro, L., Wikström, M. & Verkhovsky, M. I. Real-time electron transfer in respiratory complex I. *Proc. Natl. Acad. Sci. U.S.A.* **105**, 3763–3767 (2008).

27. Jeuken, L. J. C., Jones, A. K., Chapman, S. K., Cecchini, G. & Armstrong, F. A. Electron-transfer mechanisms through biological redox chains in multicenter enzymes. *J. Am. Chem. Soc.* **124**, 5702–5713 (2002).

28. Hubáček, M. *et al.* Strong heterologous electron sink outcompetes alternative electron transport pathways in photosynthesis. *Plant J.* **119**, 2500–2513 (2024).

29. Maxwell, K. & Johnson, G. N. Chlorophyll fluorescence—a practical guide. *J. Exp. Bot.* **51**, 659–668 (2000).

799 30. Joliot, P. & Delosme, R. Flash-induced 519 nm absorption change in green algae. *Biochim. Biophys.*
800 *Acta Bioenerg.* **357**, 267–284 (1974).

801 31. Hollis, V. S., Palacios-Callender, M., Springett, R. J., Delpy, D. T. & Moncada, S. Monitoring
802 cytochrome redox changes in the mitochondria of intact cells using multi-wavelength visible light
803 spectroscopy. *Biochim. Biophys. Acta Bioenerg.* **1607**, 191–202 (2003).

804 32. Baikie, T. K. *et al.* Photosynthesis re-wired on the pico-second timescale. *Nature* **615**, 836–840 (2023).

805 33. Diebold, L. P. *et al.* Mitochondrial complex III is necessary for endothelial cell proliferation during
806 angiogenesis. *Nat. Metab.***1**, 158–171 (2019).

807 34. Birsoy, K. *et al.* An essential role of the mitochondrial electron transport chain in cell proliferation is to
808 enable aspartate synthesis. *Cell* **162**, 540–551 (2015).

809 35. Moore, V. & Vermaas, W. Functional consequences of modification of the photosystem I/photosystem
810 II ratio in the cyanobacterium Synechocystis sp. PCC 6803. *J. Bacteriol.* **206**, (2024).

811 36. Suorsa, M. *et al.* PGR5-PGRL1-dependent cyclic electron transport modulates linear electron transport
812 rate in Arabidopsis thaliana. *Mol. Plant.* **9**, 271–288 (2016).

813 37. Malnoë, A., Wollman, F. A., De Vitry, C. & Rappaport, F. Photosynthetic growth despite a broken Q-
814 cycle. *Nat. Commun.* **2**, 1–6 (2011).

815 38. Lloyd-Laney, H. O. *et al.* Recovering biological electron transfer reaction parameters from multiple
816 protein film voltammetric techniques informed by Bayesian inference. *J. Electroanal. Chem.* **935**,
817 117264 (2023).

818 39. Bond, D. R. & Lovley, D. R. Electricity production by Geobacter sulfurreducens attached to electrodes.
819 *Appl. Environ. Microbiol.* **69**, 1548–1555 (2003).

820 40. Marsili, E. *et al.* Shewanella secretes flavins that mediate extracellular electron transfer. *Proc. Natl.*
821 *Acad. Sci. U.S.A.* **105**, 3968–3973 (2008).

822 41. Yates, M. D. *et al.* Measuring conductivity of living Geobacter sulfurreducens biofilms. *Nat.*
823 *Nanotechnol.* **11**, 910–913 (2016).

824 42. Xu, S., Barrozo, A., Tender, L. M., Krylov, A. I. & El-Naggar, M. Y. Multiheme cytochrome mediated
825 redox conduction through Shewanella oneidensis MR-1 cells. *J. Am. Chem. Soc.* **140**, 10085–10089
826 (2018).

827 43. Yang, T., Chavez, M. S., Niman, C. M., Xu, S. & El-Naggar, M. Y. Long-distance electron transport in
828 multicellular freshwater cable bacteria. *eLife* **12**, RP91097 (2024).

829 44. Light, S. H. *et al.* A flavin-based extracellular electron transfer mechanism in diverse Gram-positive
830 bacteria. *Nature* **562**, 140–144 (2018).

831 45. Bapi Kundu, B. *et al.* Extracellular respiration is a latent energy metabolism in Escherichia coli. Preprint
832 at https://www.biorxiv.org/content/10.1101/2024.05.30.596743v1 (2024).

833 46. Cereda, A. *et al.* A bioelectrochemical approach to characterize extracellular electron transfer by
834 Synechocystis sp. PCC6803. *PLoS One* **9**, e91484 (2014).

835 47. Thirumurthy, M. A. *et al.* Type IV pili-independent photocurrent production by the cyanobacterium
836 Synechocystis sp. PCC 6803. *Front. Microbiol.* **11**, 545987 (2020).

837 48. Zhang, J. Z. *et al.* Photoelectrochemistry of Photosystem II in vitro vs in vivo. *J. Am. Chem. Soc.* **19**, 31
838 (2018).

839 49. Wey, L. T. *et al.* A biophotoelectrochemical approach to unravelling the role of cyanobacterial cell
840 structures in exoelectrogenesis. *Electrochim. Acta* **395**, 139214 (2021).

841 50. Zhang, J. Z. & Reisner, E. Advancing photosystem II photoelectrochemistry for semi-artificial
842 photosynthesis. *Nat. Rev. Chem.* **4**, 6–21 (2019).

843 51. Hohmann-Marriott, M. F. & Blankenship, R. E. Evolution of photosynthesis. *Annu. Rev. Plant Biol.* **62**,
844 515–548 (2011).

845 52. Strunecký, O., Ivanova, A. P. & Mareš, J. An updated classification of cyanobacterial orders and
846 families based on phylogenomic and polyphasic analysis. *J. Phycol.* **59**, 12–51 (2023).

847 53. Flombaum, P. *et al.* Present and future global distributions of the marine Cyanobacteria
848 Prochlorococcus and Synechococcus. *Proc. Natl. Acad. Sci. U.S.A.* **110**, 9824–9829 (2013).

849 54. Perez-Boerema, A., Engel, B. D. & Wietrzynski, W. Evolution of thylakoid structural diversity. *Annu.*
850 *Rev. Cell. Dev. Biol.* **40**, 169–193 (2024).

851 55. Mullineaux, C. W. Co-existence of photosynthetic and respiratory activities in cyanobacterial thylakoid
852 membranes. *Biochim. Biophys. Acta Bioenerg.* **1837**, 503–511 (2014).

853 56. Kirchhoff, H., Mukherjee, U. & Galla, H. J. Molecular architecture of the thylakoid membrane: Lipid
854 diffusion space for plastoquinone. *Biochemistry* **41**, 4872–4882 (2002).

855 57. Komenda, J. & Barber, J. Comparison of psbO and psbH Deletion Mutants of Synechocystis PCC 6803
856 Indicates that Degradation of D1 Protein Is Regulated by the Qb Site and Dependent on Protein
857 Synthesis. *Biochemistry* **34**, 9625–9631 (1995).

858 58. Elena, Z., Norling, B., Andersson, B. & Pakrasi, H. B. Subcellular localization of the BtpA protein in
859 the cyanobacterium Synechocystis sp. PCC 6803. *Eur. J. Biochem.* **261**, 311–316 (1999).

860 59. Srivastava, R., Pisareva, T. & Norling, B. Proteomic studies of the thylakoid membrane of
861 Synechocystis sp. PCC 6803. *Proteomics* **5**, 4905–4916 (2005).

862 60. Chukhutsina, V., Bersanini, L., Aro, E. M. & Van Amerongen, H. Cyanobacterial flv4-2 operon-
863 encoded proteins optimize light harvesting and charge separation in photosystem II. *Mol. Plant.* **8**, 747–
864 761 (2015).

865 61. Cho, N. J., Frank, C. W., Kasemo, B. & Höök, F. Quartz crystal microbalance with dissipation
866 monitoring of supported lipid bilayers on various substrates. *Nat. Protoc.* **5**, 1096–1106 (2010).

867 62. Winkler, J. R. & Gray, H. B. Long-range electron tunneling. *J. Am. Chem. Soc.* **136**, 2930–2939 (2014).

868 63. Newport, T. D., Sansom, M. S. P. & Stansfeld, P. J. The MemProtMD database: a resource for
869 membrane-embedded protein structures and their lipid interactions. *Nucleic Acids Res.* **47**, D390–D397
870 (2019).

871 64. Hoyo, J., Guaus, E. & Torrent-Burgués, J. Influence of membrane galactolipids and surface pressure on
872 plastoquinone behaviour. *Bioelectrochemistry* **111**, 123–130 (2016).

873 65. Oettmeier, W. & Soll, H. J. Competition between plastoquinone and 3-(3,4-dichlorophenyl)-1,1-
874 dimethylurea at the acceptor side of Photosystem II. *Biochim. Biophys. Acta Bioenerg.* **724**, 287–290
875 (1983).

876 66. Sarewicz, M. *et al.* Catalytic reactions and energy conservation in the cytochrome bc1 and b6f
877 complexes of energy-transducing membranes. *Chem. Rev.* **121**, 2020–2108 (2021).

878 67. Lam, E. The effects of quinone analogues on cytochrome b6 reduction and oxidation in a reconstituted
879 system. *FEBS. Lett.* **172**, 255–260 (1984).

880 68. Honeycutt, R. C. & Krogmann, D. W. Inhibition of chloroplast reactions with phenylmercuric acetate.
881 *Plant Physiol.* **49**, 376–380 (1972).

882 69. Laisk, A., Oja, V., Eichelmann, H. & Dall'Osto, L. Action spectra of photosystems II and I and quantum
883 yield of photosynthesis in leaves in State 1. *Biochim. Biophys. Acta Bioenerg.* **1837**, 315–325 (2014).

884 70. Zhang, J. Z. *et al.* Competing charge transfer pathways at the photosystem II–electrode interface. *Nat.*
885 *Chem. Biol.* **12**, 1046–1052 (2016).

886 71. Itoh, S. Surface potential and reaction of membrane-bound electron transfer components. I. Reaction of
887 P-700 in sonicated chloroplasts with redox reagents. *Biochim. Biophys. Acta Bioenerg.* **548**, 579–595
888 (1979).

889 72. Hasan, S. S. *et al.* A map of dielectric heterogeneity in a membrane protein: The hetero-oligomeric
890 cytochrome b6 f complex. *J. of Phys. Chem. B* **118**, 6614–6625 (2014).

891 73. Barr, R. & Crane, F. L. Ferricyanide reduction in Photosystem II of spinach. *Plant Physiol.* **67**, 1190–
892 1194 (1981).

893 74. Teodor, A. H. & Bruce, B. D. Putting Photosystem I to work: truly green energy. *Trends Biotechnol* **38**,
894 1329–1342 (2020).

895 75. Munge, B. *et al.* Electron transfer reactions of redox cofactors in spinach Photosystem I reaction center
896 protein in lipid films on electrodes. *J. Am. Chem. Soc.* **125**, 12457–12463 (2003).

897 76. Kato, Y., Nagao, R. & Noguchi, T. Redox potential of the terminal quinone electron acceptor QB in
898 photosystem II reveals the mechanism of electron transfer regulation. *Proc. Natl. Acad. Sci. U.S.A.* **113**,
899 620–625 (2016).

900 77. Theune, M. L. *et al.* In-vivo quantification of electron flow through photosystem I – Cyclic electron
901 transport makes up about 35% in a cyanobacterium. *Biochim. Biophys. Acta Bioenerg.* **1862**, 148353
902 (2021).

903 78. Miller, N. T., Vaughn, M. D. & Burnap, R. L. Electron flow through NDH-1 complexes is the major
904 driver of cyclic electron flow-dependent proton pumping in cyanobacteria. *Biochim. Biophys. Acta*
905 *Bioenerg.* **1862**, 148354 (2021).

906 79. Ermakova, M. *et al.* Distinguishing the roles of thylakoid respiratory terminal oxidases in the
907 cyanobacterium Synechocystis sp. PCC 6803. *Plant Physiol.* **171**, 1307–1319 (2016).

908 80. Lea-Smith, D. J. *et al.* Thylakoid terminal oxidases are essential for the cyanobacterium Synechocystis
909 sp. PCC 6803 to survive rapidly changing light intensities. *Plant Physiol.* **162**, 484–495 (2013).

910 81. Buchert, F., Mosebach, L., Gäbelein, P. & Hippler, M. PGR5 is required for efficient Q cycle in the
911 cytochrome b6f complex during cyclic electron flow. *Biochem. J.* **477**, 1631–1650 (2020).

912 82. Jeuken, L. J. C. *et al.* Direct electrochemical interaction between a modified gold electrode and a
913 bacterial membrane extract. *Langmuir* **21**, 1481–1488 (2005).

914 83. Rasmussen, M. & Minteer, S. D. Investigating the mechanism of thylakoid direct electron transfer for
915 photocurrent generation. *Electrochim. Acta* **126**, 68–73 (2014).

916 84. Calkins, J. O., Umasankar, Y., O'Neill, H. & Ramasamy, R. P. High photo-electrochemical activity of
917 thylakoid–carbon nanotube composites for photosynthetic energy conversion. *Energy Environ. Sci.* **6**,
918 1891–1900 (2013).

919 85. Allen, M. J. & Crane, A. E. Null potential voltammetry - an approach to the study of Plant
920 photosystems. *Bioelectrochem. Bioenerg.* **3**, 84–91 (1976).

921 86. Cava, D. G. *et al.* Electrochemical detection of quinone reduced by Complex I Complex II and Complex
922 III in full mitochondrial membranes. *Electrochim. Acta* **484**, 144042 (2024).

923 87. McKelvey, K., Martin, S., Robinson, C. & Unwin, P. R. Quantitative local photosynthetic flux
924 measurements at isolated chloroplasts and thylakoid membranes using scanning electrochemical
925 microscopy (SECM). *J. of Phys. Chem. B* **117**, 7878–7888 (2013).

926 88. Zhao, J. *et al.* Electrochemistry of mitochondria: A new way to understand their structure and function.
927 *Electroanalysis* **20**, 1593–1598 (2008).

928 89. Pinhassi, R. I. *et al.* Photosynthetic membranes of Synechocystis or plants convert sunlight to
929 photocurrent through different pathways due to different architectures. *PLoS One* **10**, e0122616 (2015).

930 90. Seibert, M. & Kendall-Tobais, M. W. Photoelectrochemical properties of electrodes coated with
931 photoactive-membrane visicles isolated from photosynthetic bacteria. *Biochim. Biophys. Acta Bioenerg.*
932 **681**, 504–511 (1982).

933 91. Giroud, F., Nicolo, T. A., Koepke, S. J. & Minteer, S. D. Understanding the mechanism of direct
934 electrochemistry of mitochondria-modified electrodes from yeast, potato and bovine sources at carbon
935 paper electrodes. *Electrochim. Acta* **110**, 112–119 (2013).

936 92. Rasmussen, M. & Minteer, S. D. Self-powered herbicide biosensor utilizing thylakoid membranes. *Anal.*
937 *Methods* **5**, 1140–1144 (2013).

938 93. Arechederra, R. L., Waheed, A., Sly, W. S. & Minteer, S. D. Electrically wired mitochondrial electrodes
939 for measuring mitochondrial function for drug screening. *Analyst* **136**, 3747–3752 (2011).

940 94. Stanier, R. Y., Kunisawa, R., Mandel, M. & Cohen-Bazire, G. Purification and properties of unicellular
941 blue-green algae (Order Chroococcales). *Bacteriol. Rev.* **35**, 171–205 (1971).

942 95. Gorman, D. S. & Levine, R. P. Cytochrome f and plastocyanin: their sequence in the photosynthetic
943 electron transport chain of Chlamydomonas reinhardi. *Proc. Natl. Acad. Sci. U.S.A.* **54**, 1665–1669
944 (1965).

945 96. Mason, C. B., Bricker, T. M. & Moroney, J. V. A rapid method for chloroplast isolation from the green
946 alga Chlamydomonas reinhardtii. *Nat. Protoc.* **1**, 2227–2230 (2006).

947 97. Chen, Y. E., Yuan, S. & Schröder, W. P. Comparison of methods for extracting thylakoid membranes of
948 Arabidopsis plants. *Physiol. Plant.* **156**, 3–12 (2016).

949 98. Brett, C. M. A. & Oliveira Brett, A. M. *Electrochemistry: Principles, Methods, and Applications*.
950 (Oxford University Press, New York, 1993).

951 99. Porra, R. J., Thompson, W. A. & Kriedemann, P. E. Determination of accurate extinction coefficients
952 and simultaneous equations for assaying chlorophylls a and b extracted with four different solvents:
953 verification of the concentration of chlorophyll standards by atomic absorption spectroscopy. *Biochim.*
954 *Biophys. Acta Bioenerg.* **975**, 384–394 (1989).

955 100. Bennett, A. & Bogobad, L. Complementary chromatic adaptation in a filamentous blue-green alga . *J.*
956 *Cell Biol.* **58**, 419–435 (1973).

957 101. Bradford, M. M. A rapid and sensitive method for the quantitation of microgram quantities of protein
958 utilizing the principle of protein-dye binding. *Anal. Biochem.* **72**, 248–254 (1976).

959 102. Izawa, S. Acceptors and donors and chloroplast electron transport. *Methods Enzymol.* **69**, 413–434
960 (1980).

961 103. Lewis, C. M. *et al.* Electrochemically driven photosynthetic electron transport in cyanobacteria lacking
962 Photosystem II. *J. Am. Chem. Soc.* **144**, 2933–2942 (2022).

963 104. Kauny, J. & Sétif, P. NADPH fluorescence in the cyanobacterium Synechocystis sp. PCC 6803: A
964 versatile probe for in vivo measurements of rates, yields and pools. *Biochim. Biophys. Acta Bioenerg.*
965 **1837**, 792–801 (2014).

966 105. Viola, S. *et al.* Probing the electric field across thylakoid membranes in cyanobacteria. *Proc. Natl. Acad.*
967 *Sci. U.S.A.* **116**, 21900–21906 (2019).

968 106. Pettersen, E. F. *et al.* UCSF ChimeraX: Structure visualization for researchers, educators, and
969 developers. *Protein Sci.* **30**, 70–82 (2021).

970 107. Umena, Y., Kawakami, K., Shen, J. R. & Kamiya, N. Crystal structure of oxygen-evolving photosystem
971 II at a resolution of 1.9 Å. *Nature* **473**, 55–60 (2011).

108. Hasan, S. S., Yamashita, E., Baniulis, D. & Cramer, W. A. Quinone-dependent proton transfer pathways in the photosynthetic cytochrome b6f complex. *Proc. Natl. Acad. Sci. U.S.A.* **110**, 4297–4302 (2013).

109. Jordan, P. *et al.* Three-dimensional structure of cyanobacterial photosystem I at 2.5 Å resolution. *Nature* **411**, 909–917 (2001).

110. Herranen, M. *et al.* Towards functional proteomics of membrane protein complexes in Synechocystis sp. PCC 6803. *Plant Physiol.* **134**, 470–481 (2004).

Acknowledgements

This authors are grateful for support from the Biotechnology and Biological Sciences Research Council (BB/M011194/1 to J.M.L., BB/R011923/1 to J.Z.Z. & X.C.); the Worshipful Company of Leathersellers (J.M.L.); Trinity Hall, Cambridge (J.M.L.); the Novo Nordisk Foundation (NNF22OCOO79717 to L.T.W.); the Cambridge Trust (L.T.W., R.M.E. & L.N.), the Engineering and Physical Sciences Research Council (EP/R513180/1 to K.B.); Algae-UK (M.E.); the Chinese Scholarship Council (no. 202208060220 to L.N.); the Gates Cambridge Trust (D.G.K.); the Benn W Levy Trust (D.G.K.); and the Human Frontiers Science Program (LT000307/2019 to M.H.W.). The authors would like to thank Nicholas Plumeré and Henry Lloyd-Laney for helpful discussions.

Author information

Authors and Affiliations:

Department of Biochemistry, University of Cambridge, Cambridge, UK – Joshua M. Lawrence, Darius Kosmützky, Christopher J. Howe.

Yusuf Hamied Department of Chemistry, University of Cambridge, UK – Joshua M. Lawrence, Rachel M. Egan, Mairi Eyres, Lan Nan, Jenny Z. Zhang.

Molecular Plant Biology, Department of Life Technologies, University of Turku, Turku, Finland – Laura T. Wey.

Department of Chemical Engineering and Biotechnology, University of Cambridge, Cambridge, UK – Karan Bali.

Department of Mechanical, Materials and Manufacturing Engineering, University of Nottingham, Nottingham, UK – Xiaolong Chen.

Niels Bohr Institute, University of Copenhagen, Copenhagen, Denmark – Mary H. Wood.

Department of Biochemistry, University of Rostock, Rostock, Germany – Marc M. Nowaczyk.

Contributions:

J.M.L., L.T.W., C.J.H. and J.Z.Z. developed the idea of interfacing cyanobacterial thylakoid membranes with electrodes. J.M.L. developed the platform as an analytical tool. J.M.L designed and performed the experiments under the supervision of C.J.H. and J.Z.Z.. R.M.E. optimised the electrodes, in addition to fabricating electrodes and performing SEM alongside X.C and L.N. K.B. performed the nanoparticle tracking analysis. L.N. assisted with oxygen evolution measurements. M.E. and D.G.K. performed algal thylakoid membrane extractions. M.H.W. assisted with QCM-D measurements. J.M.L. wrote the manuscript, with editing from C.J.H and J.Z.Z and input from all authors.

Authors and Affiliations:

Correspondence to Christopher J. Howe (ch26@cam.ac.uk) and Jenny Z. Zhang (jz366@cam.ac.uk).

1016 **Ethics declaration**

1017 The authors declare no competing interests.

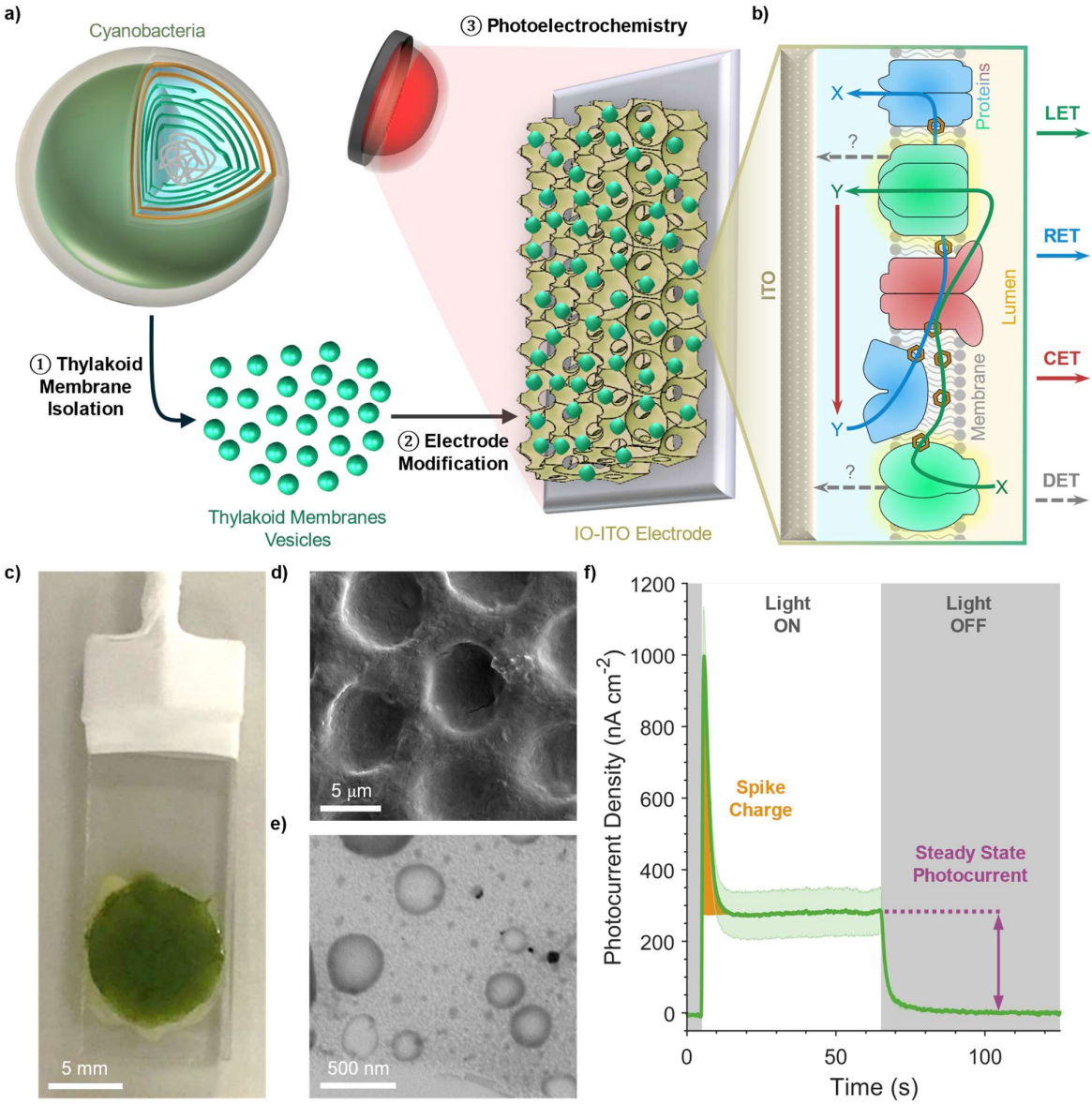

Figure 1: Quantitative measurements of thylakoid membrane photocurrents
a) Experimental workflow of thylakoid membrane electrochemistry experiments. IO-ITO, inverse opal-indium tin oxide. **b)** Schematic depicting the electron transport network of cyanobacterial thylakoid membranes interfaced with the electrode. The thylakoid membrane electron transport pathways can be measured due to electron transfer between their components and the electrode. More detailed diagrams of thylakoid membrane electron transport chains can be seen in Fig. 2a and 3a. **c)** Picture, and **d)** SEM micrograph of a *Synechocystis* thylakoid membrane-modified electrode. **e)** STEM micrograph of isolated thylakoid membranes. **f)** Example thylakoid membrane photocurrent profiles, with key parameters labelled. All photocurrent measurements, including this, were performed under standard conditions (Methods), unless stated otherwise. Data presented as the mean of biological replicates ± S.E.M. ($n = 3$). CET, cyclic electron transport; DET, direct electron transfer; IO-ITO, inverse opal-indium tin oxide; LET, linear photosynthetic electron transport; RET, respiratory electron transport.

1032

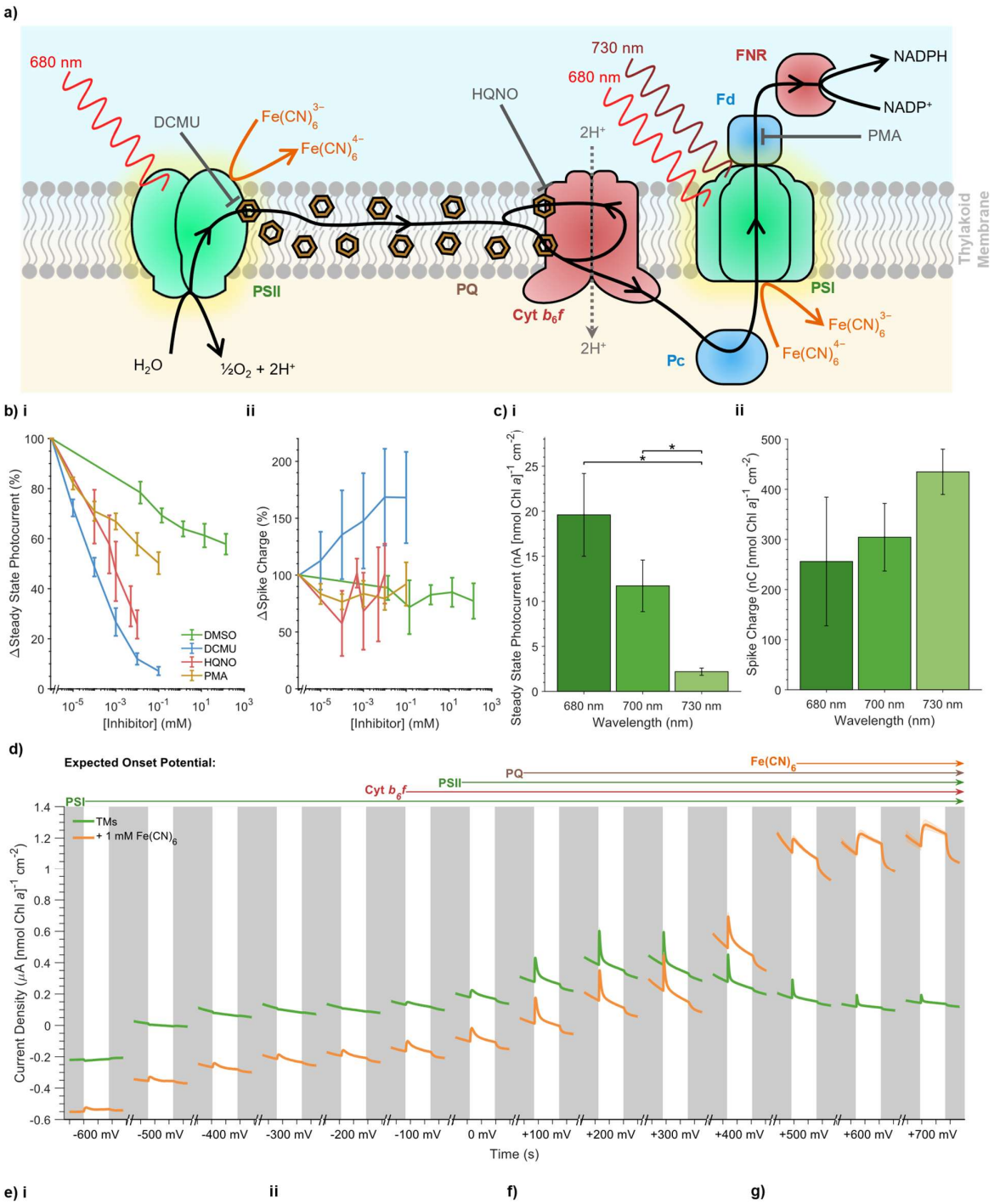
a)
680 nm
DCMU
Fe(CN)6 3−
Fe(CN)6 4−
HQNO
730 nm
680 nm
FNR
NADPH
NADP+
Fd
PMA
2H+
Thylakoid Membrane
PSII
PQ
Cyt b6f
PSI
Fe(CN)6 3−
Fe(CN)6 4−
Pc
H2O
½O2 + 2H+
b) i
ii
ΔSteady State Photocurrent (%)
ΔSpike Charge (%)
[Inhibitor] (mM)
DMSO
DCMU
HQNO
PMA
c) i
ii
Steady State Photocurrent (nA [nmol Chl a]-1 cm-2)
Spike Charge (nC [nmol Chl a]-1 cm-2)
680 nm
700 nm
730 nm
Wavelength (nm)
d)
Expected Onset Potential:
Fe(CN)6
PQ
PSII
Cyt b6f
PSI
TMs
+ 1 mM Fe(CN)6
Current Density (μA [nmol Chl a]-1 cm-2)
-600 mV
-500 mV
-400 mV
-300 mV
-200 mV
-100 mV
0 mV
+100 mV
+200 mV
+300 mV
+400 mV
+500 mV
+600 mV
+700 mV
Time (s)
e) i
ii
f)
g)
Steady State Photocurrent (nA [nmol Chl a]-1 cm-2)
Spike Charge (μC [nmol Chl a]-1 cm-2)
Potential (mV vs SHE)
TMs
+ 1 mM Fe(CN)6
TMs + 1% DMSO
+ 100 μM DCMU
+ 10 μM HQNO
Spike Charge (nC [nmol Chl a]-1 cm-2)
50 μmol m-2 s-1
730 nm
500 μmol m-2 s-1
680 nm
Pretreatment

1033 **Figure 2: Photosynthetic electron transport pathways influence thylakoid membrane**
1034 **photocurrents**
1035 **a)** Schematic depicting the linear photosynthetic electron transport pathway of *Synechocystis*
1036 thylakoid membranes. The sites of action of inhibitors, electron mediators and wavelengths of light are
1037 shown. **b)** Effect of various inhibitors of photosynthetic electron transport on the relative change of
1038 photocurrent parameters. DMSO alone is included as a control. **c)** Effect of illumination wavelength on
1039 photocurrent parameters. Supporting data in Supplementary Fig. 6. **d)** Stepped chronoamperometry
1040 scan of thylakoid membranes, with each successive photocurrent recorded at an increasing E_{app} value
1041 (mV vs SHE) and in the absence and presence of 1 mM $Fe(CN)_6$ along with an enzymatic oxygen
1042 removal systems (1 mM glucose, 100 µg mL^{-1} glucose oxidase, 50 µg mL^{-1} catalase). X-axis tick
1043 spacings represent 20 s of experimental time. **e)** Photocurrent parameters calculated from **d**. **f)** Effect
1044 of E_{app} and photosynthetic inhibitors on Steady State Photocurrents, calculated from stepped
1045 chronoamperometry experiments performed without enzymatic oxygen removal. Supporting data in
1046 Supplementary Fig. 7-8. **g)** Effect of light pre-treatment conditions on Spike Charge, calculated from
1047 photocurrents recorded after 10 s of pretreatment followed by 10 s of darkness. Supporting data in
1048 Supplementary Fig. 10. Sub-panels depict measurements of **(i)** Steady State Photocurrent and **(ii)**
1049 Spike Charge magnitudes. All data presented as the mean of biological replicates ± S.E.M. ($n = 3$). p-
1050 values calculated using two-tailed unpaired t-tests (*** $p \leq 0.001$, ** $0.001 < p \leq 0.01$, $p \leq 0.05$). Chl,
1051 chlorophyll; Cyt b_6f, cytochrome b_6f; DCMU, 3-(3,4-dichlorophenyl)-1,1-dimethylurea; DMSO, dimethyl
1052 sulfoxide; Fd, ferredoxin; $Fe(CN)_6^{3-}/Fe(CN)_6^{4-}$, ferri-/ferrocyanide redox couple; FNR, ferredoxin-
1053 $NADP^+$ reductase; HQNO, N-oxo-2-heptyl-4-Hydroxyquinoline; Pc, plastocyanin; PQ, plastoquinone;
1054 PSII, photosystem II; PSI, photosystem I; NADP(H), nicotinamide adenine dinucleotide phosphate;
1055 PMA, phenylmercuric acetate; SHE, standard hydrogen electrode; TM, thylakoid membrane.

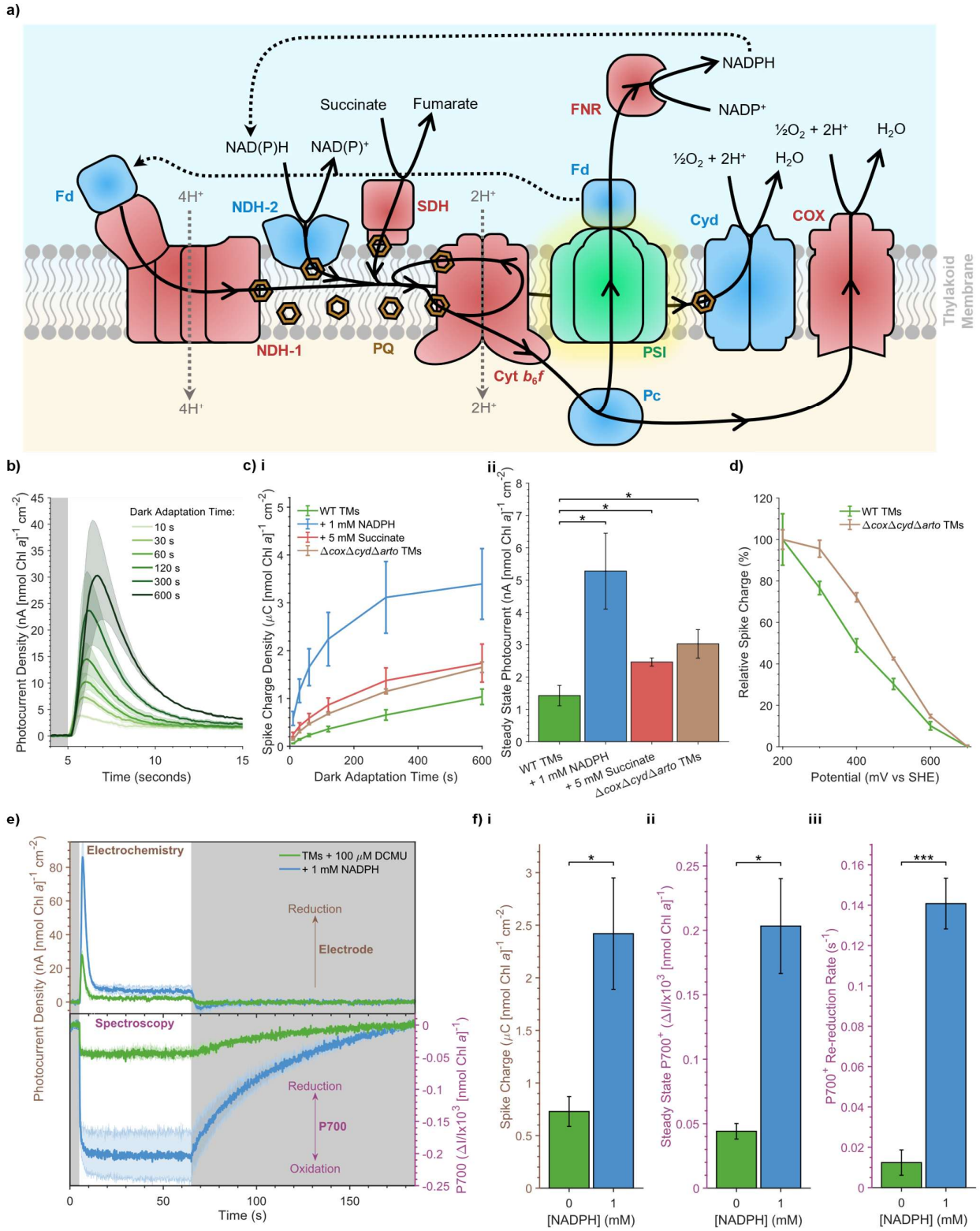

Figure 3: Electrochemical measurements of light-independent plastoquinone reduction **a)** Schematic depicting the cyclic and respiratory electron transport pathways of *Synechocystis* thylakoid membranes. **b)** Thylakoid membrane photocurrent profiles recorded in increasing dark adaptation times. **c)** The effect of dark adaptation time on photocurrent parameters recorded in conditions with a more reduced plastoquinone pool. This was achieved by addition of substrates which reduce plastoquinone via dehydrogenases (succinate and NADPH) or by utilising a mutant

1062 lacking respiratory terminal oxidases which oxidise the plastoquinone pool (Δ*cyd*Δ*cox*Δ*arto*). Sub-
1063 panels depict measurements **(i)** Spike Charge (at all dark adaptation times) and **(ii)** Steady State
1064 Photocurrents (at a dark adaptation time of 60 s) are shown, with the legend shared between both
1065 panels. Supporting data in Supplementary Fig. 11. **d)** The relative decay in Spike Charge measured
1066 at E_{app} values ≥ +200 mV vs SHE for thylakoid membrane from wild type and Δ*cyd*Δ*cox*Δ*arto* cells
1067 without enzymatic oxygen removal. Supporting data in Supplementary Fig. 12. **e)** *In operando*
1068 measurements of thylakoid membrane photocurrents alongside the oxidation of the P700 reaction
1069 centre of photosystem I, measured in the absence and presence of 1 mM NADPH. **g)** Measurements
1070 of **(i)** Spike Charge, **(ii)** steady state P700 oxidation, and **(iii)** P700 re-reduction rate calculated from
1071 data in panel **f**. All experiments performed in the presence of 100 μM DCMU. All data presented as
1072 the mean of biological replicates ± S.E.M. ($n = 3$). p-values calculated using two-tailed unpaired t-tests
1073 (*** $p \leq 0.001$, ** $0.001 < p \leq 0.01$, $p \leq 0.05$). Chl, chlorophyll; COX, cytochrome *c* oxidase; Cyd,
1074 cytochrome *bd* oxidase; Cyt b_6f, cytochrome b_6f; Fd, ferredoxin; DCMU, 3-(3,4-dichlorophenyl)-1,1-
1075 dimethylurea; FNR, ferredoxin-$NADP^+$ reductase; NAD(P)(H), nicotinamide adenine dinucleotide
1076 (phosphate); NDH-1, type I NAD(P)H dehydrogenase; NDH-2, type II NAD(P)H dehydrogenase; Pc,
1077 plastocyanin; PQ, plastoquinone; PSI, photosystem I; SDH, succinate dehydrogenase; SHE, standard
1078 hydrogen electrode; TM, thylakoid membrane; WT, wild type.

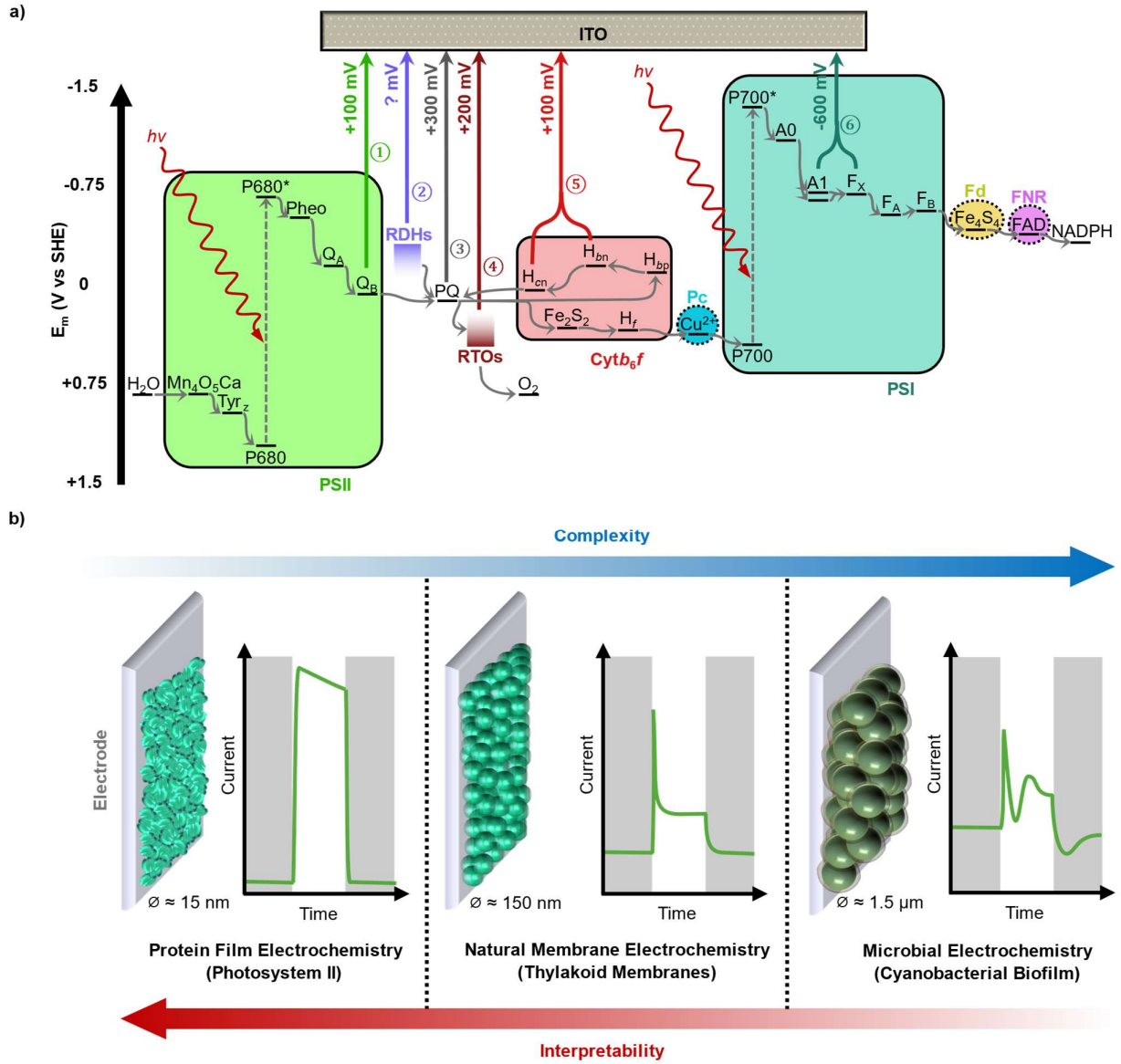

Figure 4: Evaluation of thylakoid membrane electrochemistry
a) Identified thylakoid membrane-electrode electron transport pathways. Redox potentials[2] and suspected routes of electron transport between electron transport cofactors and the electrode are shown. Supporting information in Supplementary Table 1. **b)** Schematic showing photocurrent measurements of electrodes modified with cyanobacterial photosystems, thylakoid membranes and biofilms. An approximate diameter is shown for each analyte. Representations of the photocurrent profile are depicted, showing trade-offs between the complexity and interpretability of these data[50]. A, acceptor; Cyt *b*$_6$*f*, cytochrome *b*$_6$*f*; F, Fe-S cluster; FAD, flavin adenine dinucleotide; Fd, ferredoxin; FNR, ferredoxin-NADP$^+$ reductase; H, haem; ITO, indium tin oxide; NADP(H), nicotinamide adenine dinucleotide phosphate; P, primary donor; Pc, plastocyanin; Pheo, pheophytin; PQ, plastoquinone; PSII, photosystem II; PSI, photosystem I; Q, quinone; RDHs, respiratory dehydrogenases; RTOs, respiratory terminal oxidases; SHE, standard hydrogen electrode; Tyr, tyrosine.

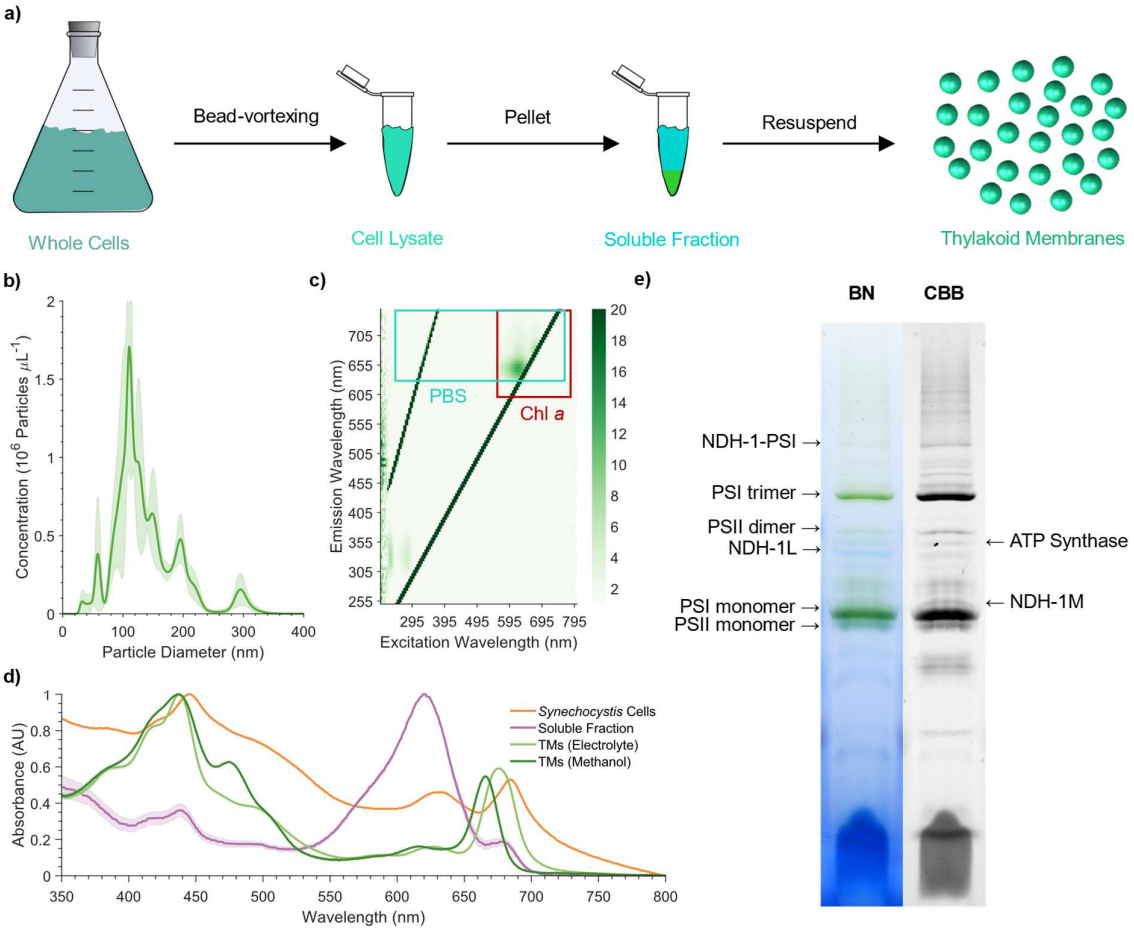

Extended Data Figure 1: Isolation of cyanobacterial thylakoid membrane vesicles. **a)** Protocol for cyanobacterial thylakoid membrane isolation. Characterisation of thylakoid membranes isolated from *Synechocystis*. **b)** Size distribution measured by NTA, **c)** fluorescence excitation-emission matrix (Supporting data in Supplementary Fig. 1a), **d)** absorbance spectra, and **e)** BN-PAGE, with putative assignments of protein bands are labelled[110] (Supporting data in Supplementary Fig. 2). NTA and absorbance data presented as the mean of biological replicates ± S.E.M. (*n* = *3*). Other results (*n* = 1). BN, blue native; CBB, Coomassie brilliant blue; Chl *a*, chlorophyll *a*; NDH-1, type-I NAD(P)H dehydrogenase; PBS, phycobilisome; PSII, photosystem II; PSI, photosystem I; TM, thylakoid membrane.

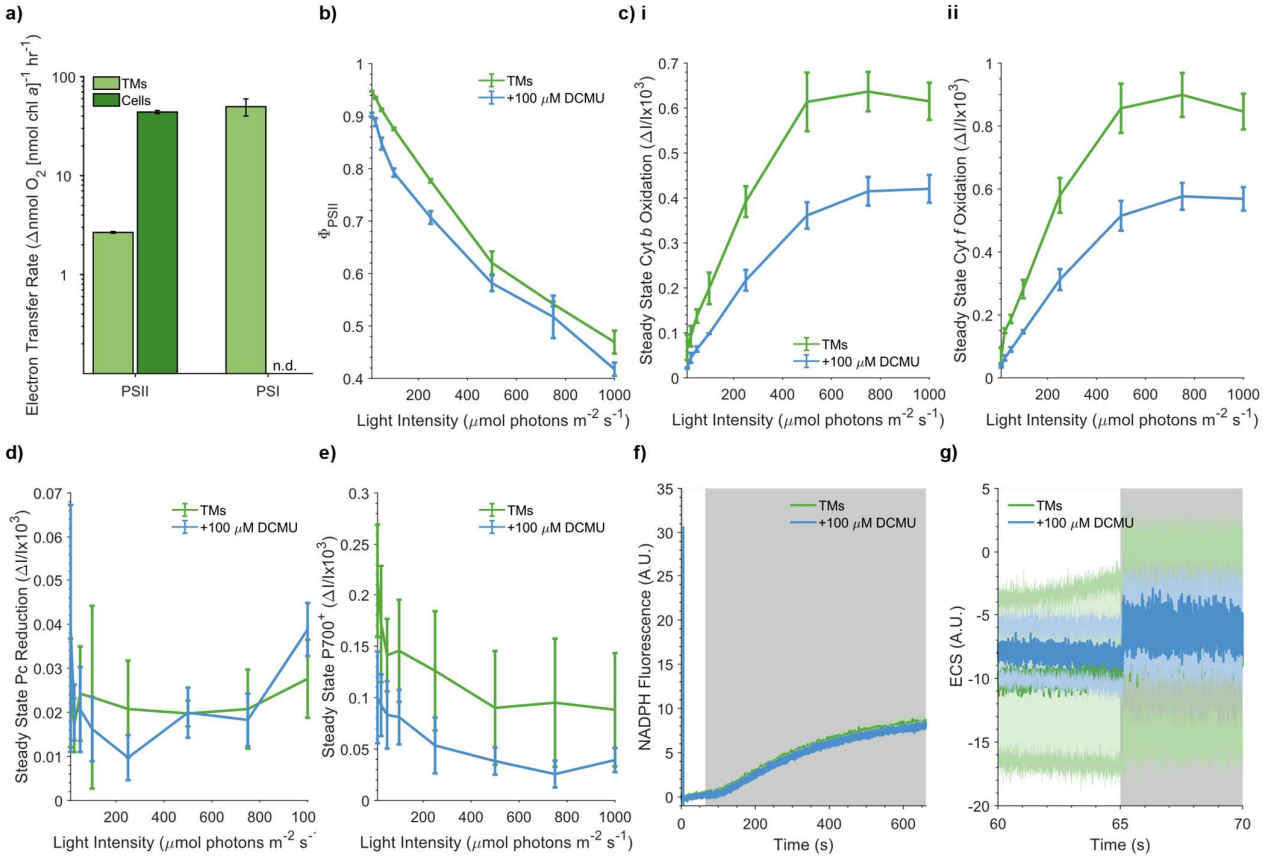

Extended Data Figure 2: Photosynthetic activity of isolated thylakoid membranes. **a)** Oxygen evolution rates performed under conditions to measure the maximal activity of PSII and PSI activity recorded under 1500 µmol m^{-2} s^{-1} of 680 nm light. PSII measurements were performed in the presence of 1 mM DCBQ and 1 mM ferricyanide as electron acceptors. PSI measurements were performed in the presence of 100 µM DCMU, 4 mM MV as an electron acceptor, and 20 mM ascorbate and 200 µM DCPIP as electron donors. **b)** ϕ_{PSII} and **c)** cytochrome *b*, and **d)** cytochrome *f* oxidation recorded at sequentially increasing intensities of 630 nm light, with 1 mM ferri-/ferrocyanide redox couple as an electron acceptor. **d)** Plastocyanin and **e)** P700 oxidation recorded at sequentially increasing intensities of 630 nm light, with 1 mM MV as an electron acceptor. **f)** NADPH fluorescence recorded at 500 µE with 1 mM $NADP^+$ as an electron acceptor. **g)** ECS measurements recorded at 500 µE with 1 mM ferri-/ferrocyanide redox couple as an electron acceptor. All spectroscopic measurements were performed with 630 nm light in the absence and presence of 100 µM DCMU, with chopped light (1 min on 1 min off), with the exception of NADPH fluorescence measurements (1 min on 10 min off). All data presented as the mean of biological replicates ± S.E.M. (*n* = *3*). Chl, chlorophyll; Cyt, cytochrome; DCMU, 3-(3,4-dichlorophenyl)-1,1-dimethylurea; ECS, electrochromic shift; NADP(H), nicotinamide adenine dinucleotide phosphate; Pc, plastocyanin; PSII, photosystem II; PSI, photosystem I; TM, thylakoid membrane.

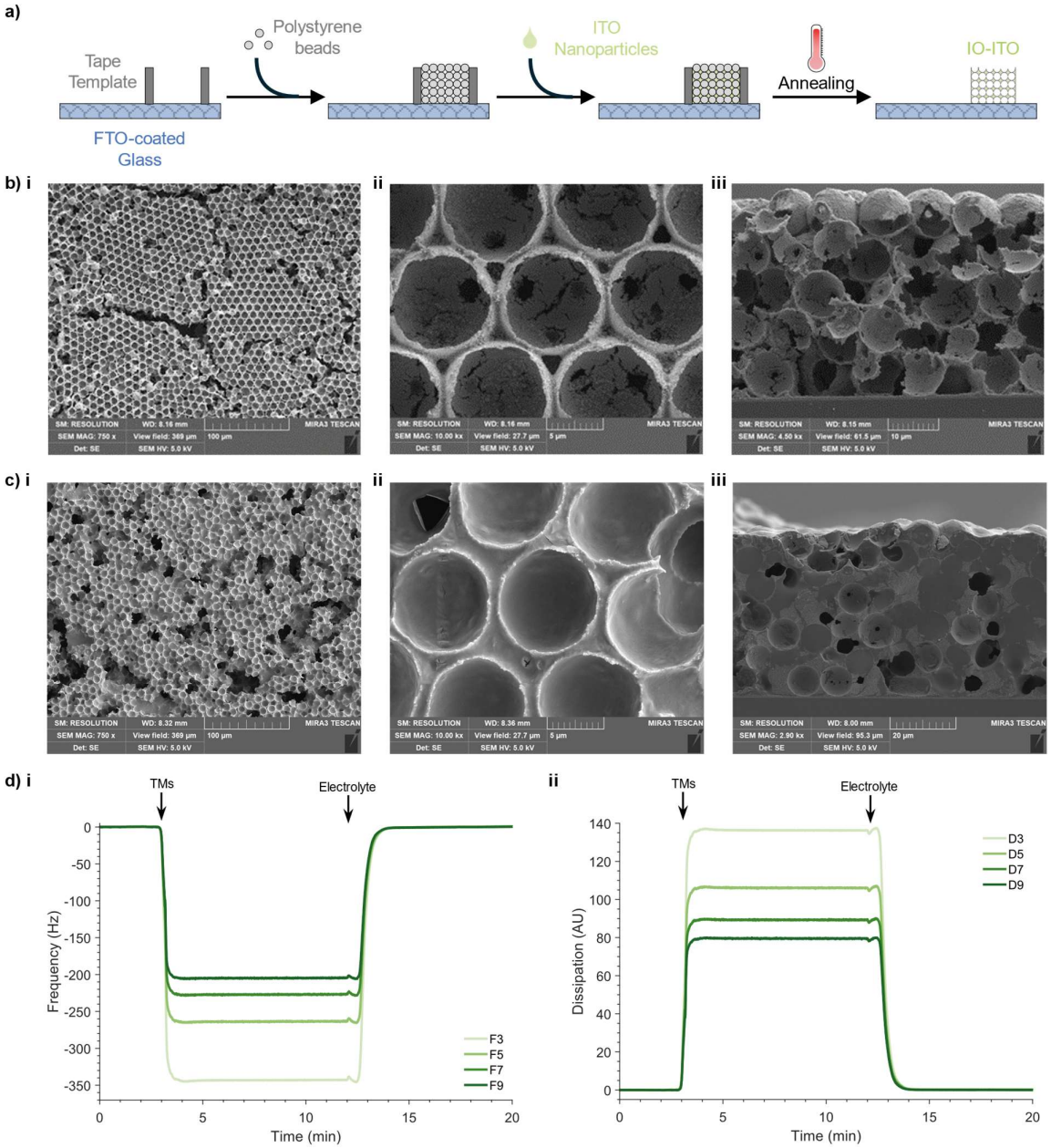

Extended Data Figure 3: Fabrication of thylakoid membrane-modified IO-ITO electrodes. **a)** Protocol for IO-ITO electrode fabrication. SEM images of **b)** unmodified IO-ITO electrodes, and **c)** IO-ITO electrodes modified with thylakoid membranes with a loading of 20 µg chlorophyll *a*. **(i-ii)** Top views at two magnifications, and **(iii)** a cross section are shown. Supporting data in Supplementary Fig. 3. **d)** QCM-D measurements of thylakoid membrane vesicles binding to ITO, showing simultaneous measurements of **(i)** frequency and **(ii)** dissipation. (*n* = *1*). FTO, fluorine-doped tin oxide; IO-ITO, inverse opal-indium tin oxide; TM, thylakoid membrane.

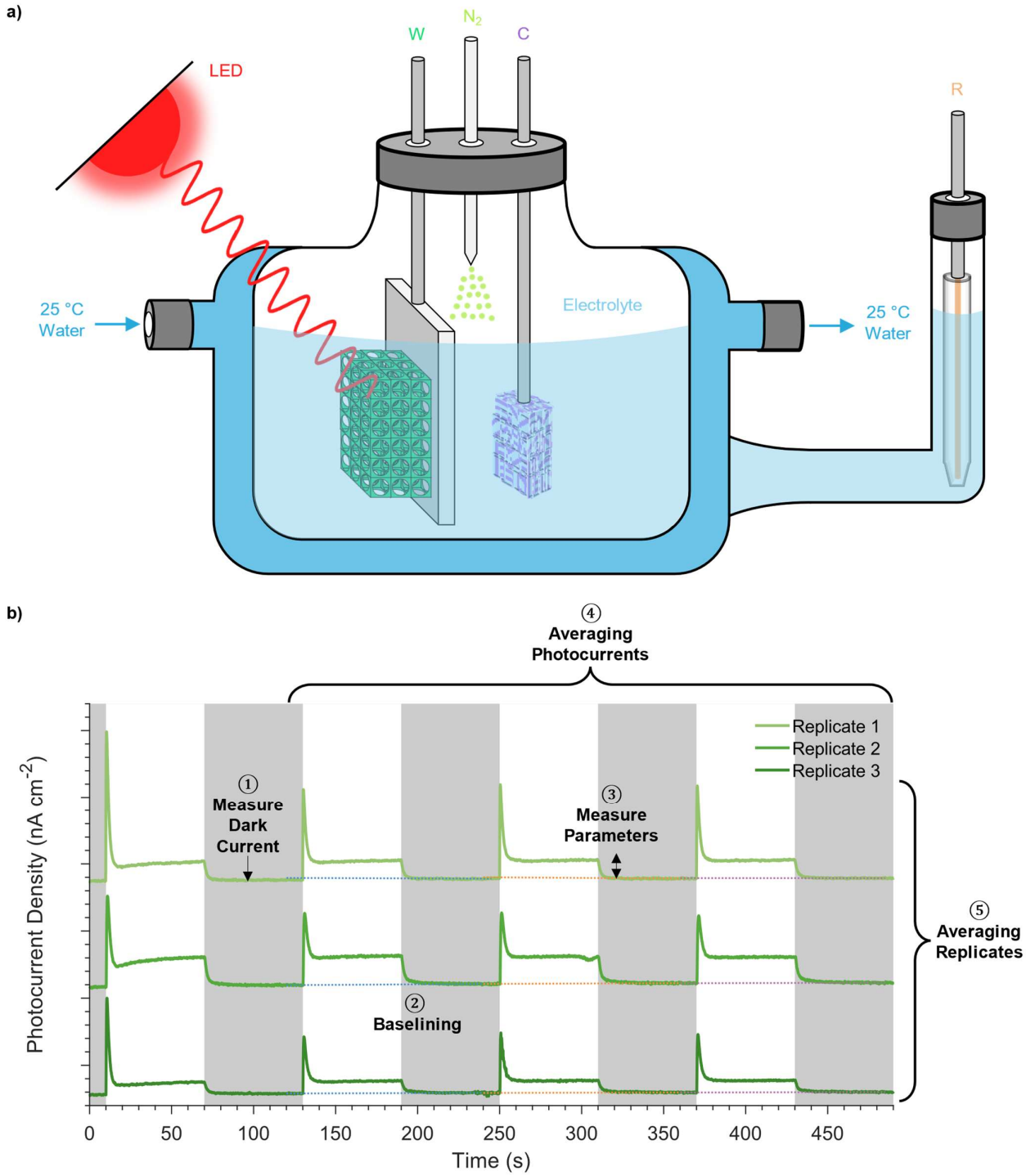

Extended Data Figure 4: Collection and analysis of thylakoid membrane photoelectrochemistry data.
a) Schematic of the photo-bioelectrochemical cell used to record thylakoid membrane photocurrents. Photographed in Supplementary Fig. 4. **b)** Processing of thylakoid membrane chronoamperometry data. Chronoamperometry scans were recorded from multiple biological replicates under chopped light, with grey periods representing darkness and white periods light. Depicted scans were obtained from three biological replicates under standard conditions. Y-axis shown is a relative scale, with minor ticks representing 200 nA cm^{-2}. Data processing steps are labelled: ① dark current calculation, ②

1136 baselining, ③ parameter calculation, ④ averaging of successive photocurrent measurements, ⑤
1137 averaging of biological replicates. Full details of data processing are included in Supplementary Note
1138 2. C, counter electrode; R, reference electrode; W, working electrode.

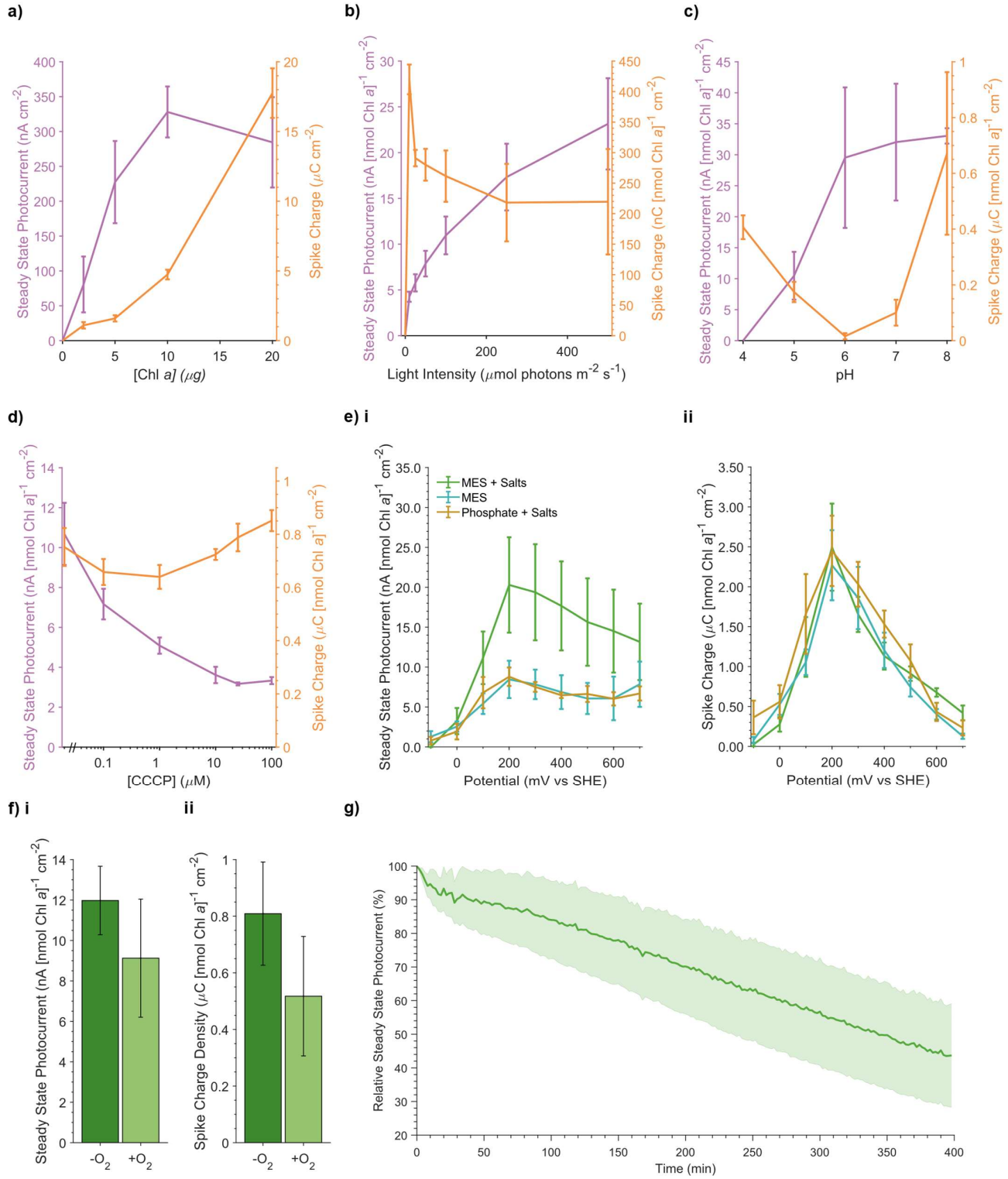

Extended Data Figure 5: Effect of experimental conditions on thylakoid membrane photocurrents.
Effect of **a)** chlorophyll a loading, **b)** light intensity, **c)** pH (Supporting data in Supplementary Fig. 5) and **d)** the ionophore CCCP on photocurrent parameters. **e)** Effect of electrolyte composition and E_{app} on photocurrent parameters. Electrolyte was composed of either 50 mM MES or potassium

1145 phosphate, supplemented with or without salts (15 mM NaCl, 5 mM $MgCl_2$, 2 mM $CaCl_2$).**f)** Effect of
1146 the presence of oxygen on photocurrent parameters. Oxygen was removed through purging with N_2
1147 gas. Sub-panels depict measurements of **(i)** Steady State Photocurrent and **(ii)** Spike Charge
1148 magnitudes. **g)** Relative change in Steady State Photocurrent recorded from successive photocurrent
1149 measurements performed over 400 min. All data presented as the mean of biological replicates ±
1150 S.E.M. ($n = 3$). p-values calculated using two-tailed unpaired t-tests (*** $p \leq 0.001$, ** $0.001 < p \leq 0.01$,
1151 $p \leq 0.05$). Chl, chlorophyll; CCCP, Carbonyl cyanide m-chlorophenyl hydrazone; DCMU, 3-(3,4-
1152 dichlorophenyl)-1,1-dimethylurea; MES, 2-(N-morpholino)ethanesulfonic acid; SHE, standard
1153 hydrogen electrode.

1154

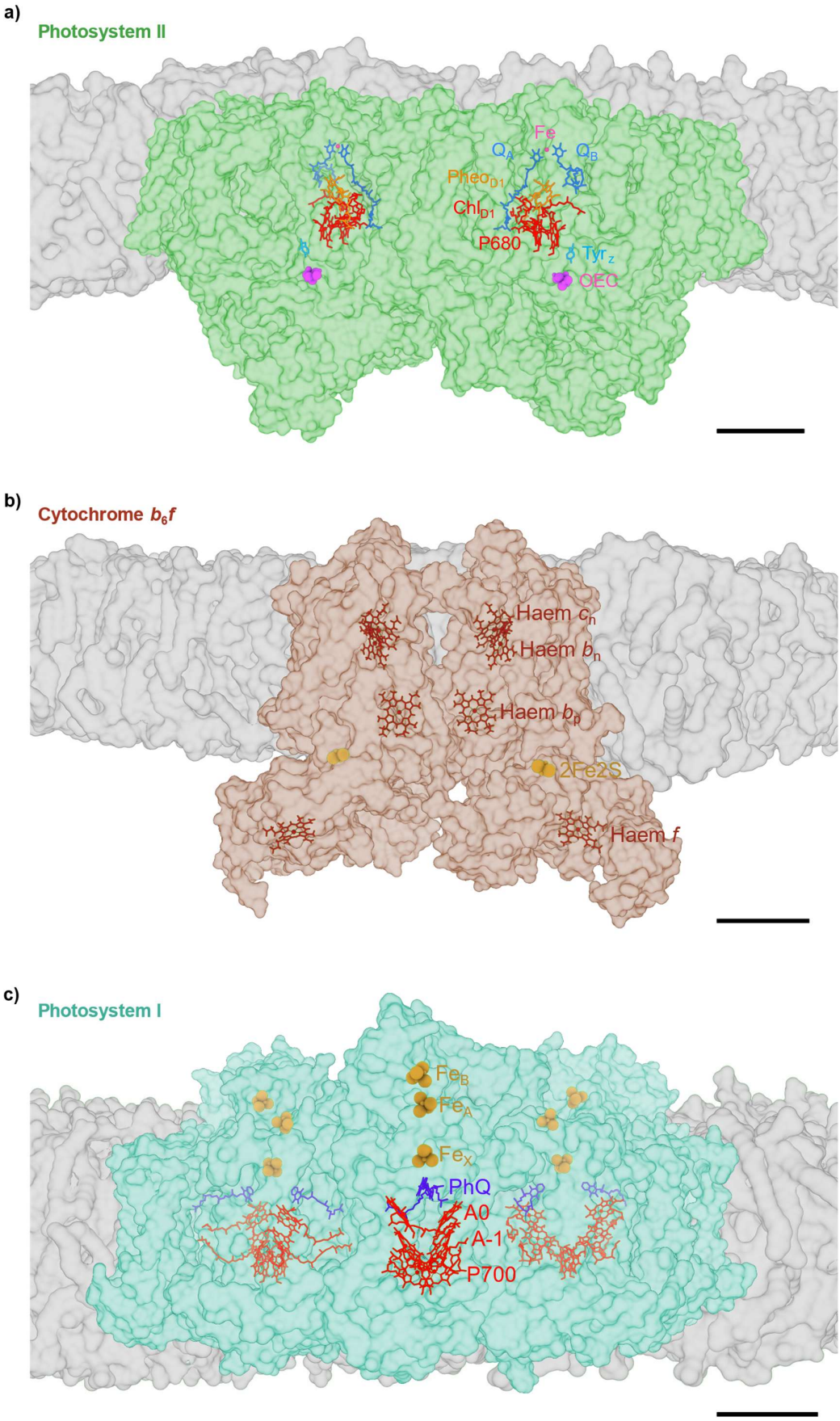
a)
Photosystem II
Fe
Q_A
Q_B
$Pheo_{D1}$
Chl_{D1}
P680
Tyr_z
OEC
b)
Cytochrome b_6f
Haem c_n
Haem b_n
Haem b_p
2Fe2S
Haem f
c)
Photosystem I
Fe_B
Fe_A
Fe_X
PhQ
A0
A-1
P700

1155 **Extended Data Figure 6: Structural analysis of thylakoid membrane protein complexes**
1156 **embedded in a lipid bilayer.**
1157 Structural models of **a)** photosystem II dimer (PDB: 3WU2[107]), **b)** cytochrome b_6f dimer (PDB:
1158 4H44[108]), and **c)** photosystem I trimer (PDB: 1JBO[109]). Insertion of these biological assemblies into
1159 lipid bilayers was predicted by molecular dynamics simulations, as part of the MemProtDB resource[63].
1160 Front views are shown. Scale bar: 2nm. A, acceptor; Chl, chlorophyll; Fe, iron-sulphur cluster; 2Fe2S,
1161 Rieske iron-sulphur cluster; OEC, oxygen evolving complex; P, primary donor; Ph, phylloquinone;
1162 Pheo, pheophytin; Q, quinone; Tyr, tyrosine.

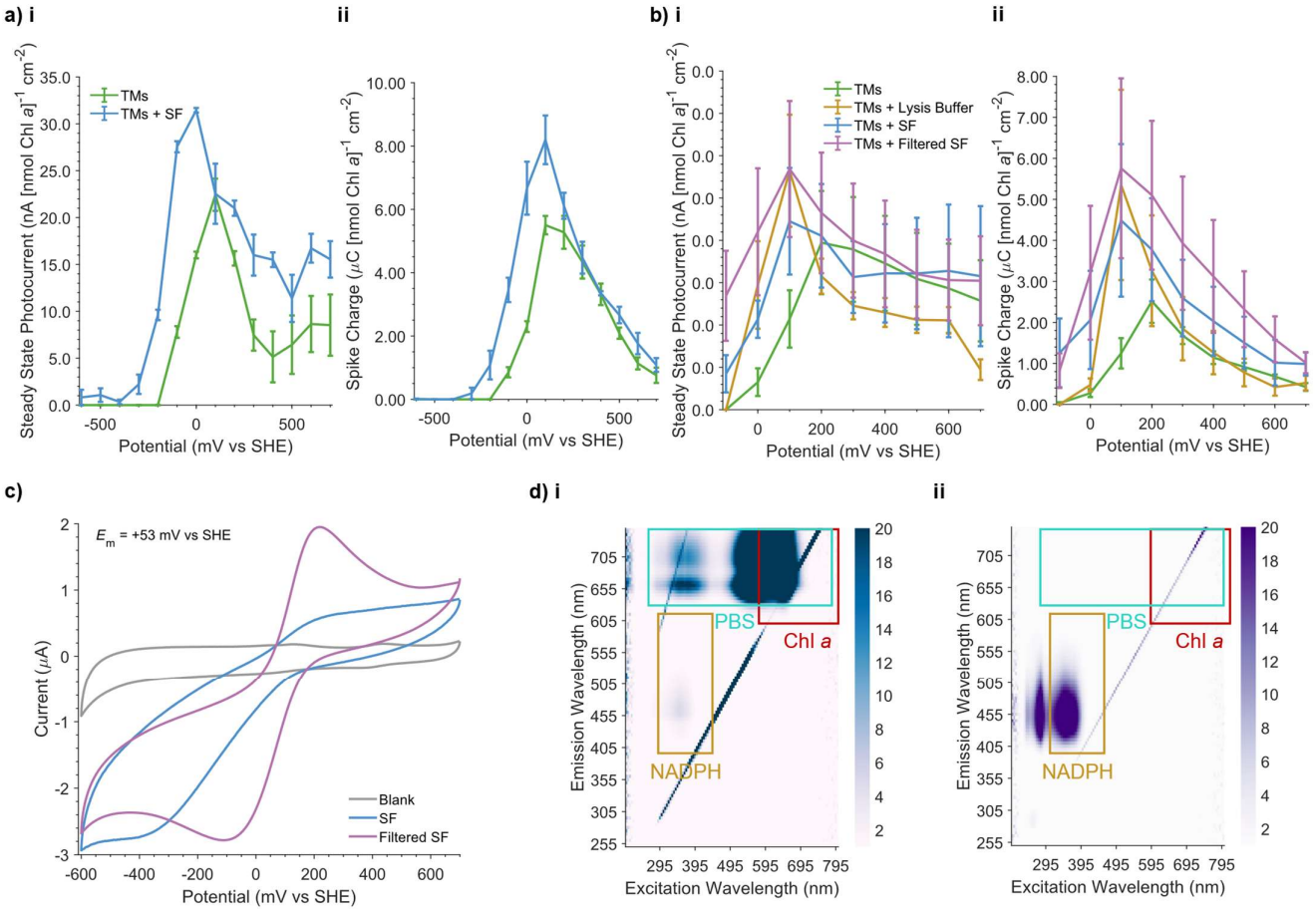

Extended Data Figure 7: Effect of soluble protein and metabolites on thylakoid membrane photocurrents.
a) Effect of soluble fraction on photocurrent parameters, recorded at increasing E_{app} values with an enzymatic oxygen removal system (1 mM glucose, 100 µg mL^{-1} glucose oxidase, 50 µg mL^{-1} catalase). **b)** Effect of lysis buffer, soluble fraction and 3 kDa-filtered soluble fraction on photocurrent parameters, recorded at increasing E_{app} values in the absence of enzymatic oxygen removal. Sub-panels depict measurements of **(i)** Steady State Photocurrent and **(ii)** Spike Charge magnitudes. Supporting data in Supplementary Fig. 9. Electrochemical data presented as the mean of biological replicates ± S.E.M. (*n = 3*). **c)** Cyclic voltammetry of soluble fraction and 3 kDa-filtered soluble performed with an ITO-coated glass working electrode, platinum mesh counter electrode and Ag/AgCl reference electrode with a scan rate of 10 mV s^{-1}. Supporting data in Supplementary Fig. 7. (*n = 1*). **d)** Fluorescence excitation emission matrices of **(i)** soluble fraction and **(ii)** 3 kDa-filtered soluble fraction. Supporting data in Supplementary Fig. 1b. (*n = 1*). Chl, chlorophyll; NADP(H), nicotinamide adenine dinucleotide phosphate; FSF, 3 kDa-filtered soluble fraction; PBS, phycobilisomes; SF, soluble fraction; SHE, standard hydrogen electrode; TM, thylakoid membrane.

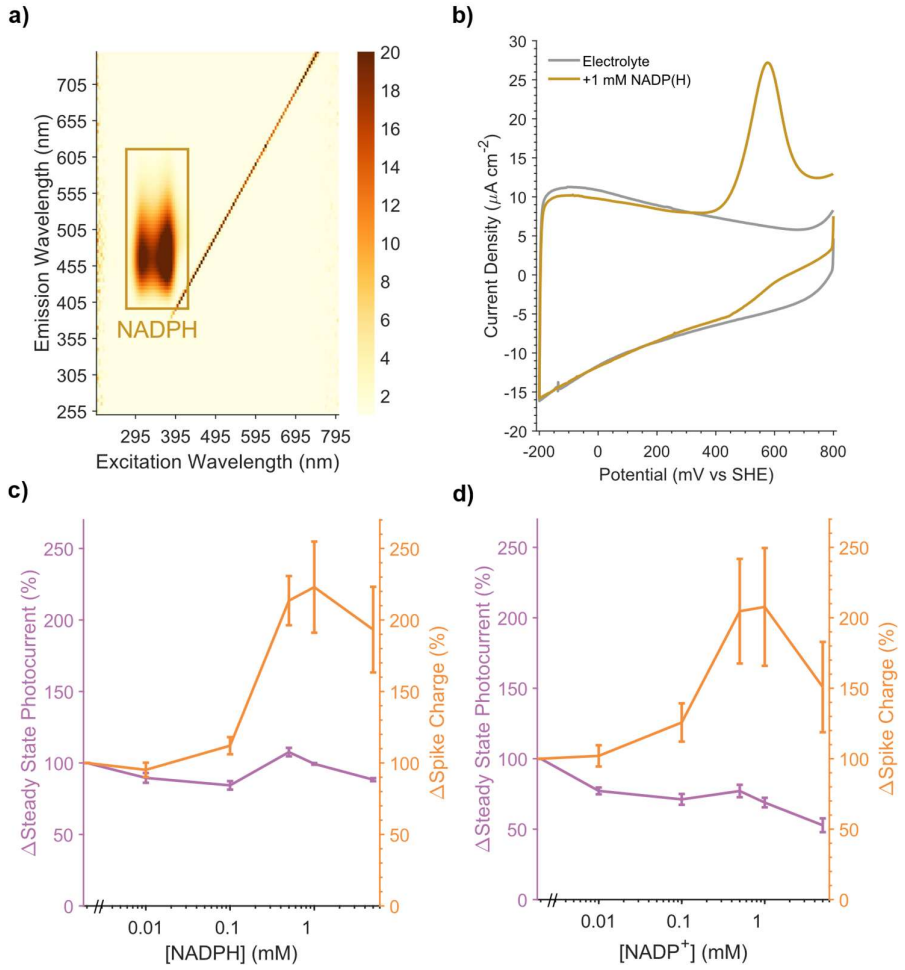

Extended Data Figure 8: Effect of NADP(H) on thylakoid membrane photocurrents. **a)** Fluorescence excitation emission matrices of NADPH. (*n = 1*). Supporting data in Supplementary Fig. 1c. **b)** Cyclic voltammogram of NADP(H), performed with an IO-ITO working electrode, platinum mesh counter electrode and Ag/AgCl reference electrode, in electrolyte buffer supplemented with 2.5 mM of $NADP^+$ and 2.5 mM of NADPH, using a scan rate of 2 mV s^{-1}. (*n = 1*). Effect of **c)** $NADP^+$ and **d)** NADPH addition on relative photocurrent parameters. Sub-panels depict measurements of **(i)** Steady State Photocurrent and **(ii)** Spike Charge magnitudes. Electrochemical data presented as the mean of biological replicates ± S.E.M. (*n = 3*). NADP(H), nicotinamide adenine dinucleotide phosphate; SHE, standard hydrogen electrode.

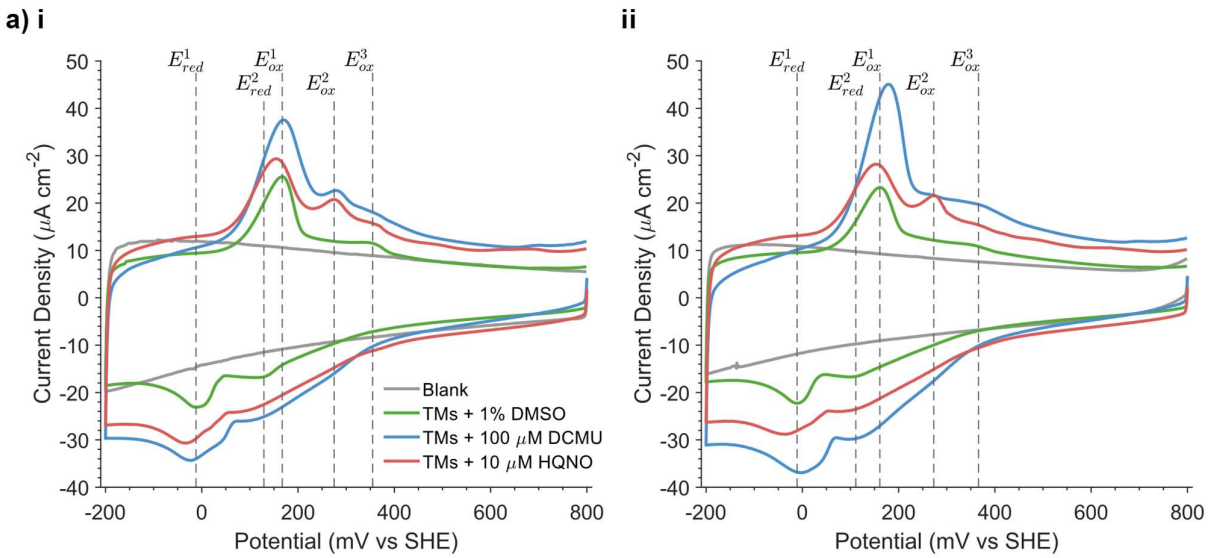

b)

Peaks	+DMSO		+DCMU		+HQNO	
(mV vs SHE)	D	L	D	L	D	L
†E^1_{red}	-12	-11	-24	-2	-34	-36
‡E^2_{red}	+129	+111	+129	+117	+129	+111
†E^1_{ox}	+167	+161	+170	+179	+167	+153
†E^2_{ox}	/	/	+279	/	+275	+273
‡E^3_{ox}	+355	/	/	/	+366	+367

Q_B / $PQ(H_2)$ [E_m = ~+77 mV]

Extended Data Figure 9: Identifying redox cofactors with cyclic voltammetry.
a) Cyclic voltammograms of thylakoid membranes recorded in electrolyte buffer supplemented with DMSO (1 %), DCMU (100 µM) and HQNO (10 µM), alongside blank measurements recorded without thylakoid membranes. Experiments were performed with an IO-ITO working electrode, platinum mesh counter electrode and Ag/AgCl reference electrode, using a scan rate of 2 mV s^{-1}. Identifiable oxidation and reduction peaks are labelled. Sub-panels depict measurements recorded **(i)** in darkness and **(ii)** under 50 µmol m^{-2} s^{-1} of 680 nm light. **b)** The potentials of oxidation and reduction peaks measured from **a**. Potentials measured through a peak search algorithm are denoted with †, whilst potentials measured manually are denoted with ‡. Peaks E^1_{Red} and E^1_{Ox} are consistent with a redox couple for Q_B in PSII and/or $PQ(H_2)$[2]. D, dark; DCMU, 3-(3,4-dichlorophenyl)-1,1-dimethylurea; DMSO, dimethyl sulfoxide; HQNO, N-oxo-2-heptyl-4-Hydroxyquinoline; L, light; SHE, standard hydrogen electrode; TM, thylakoid membrane.

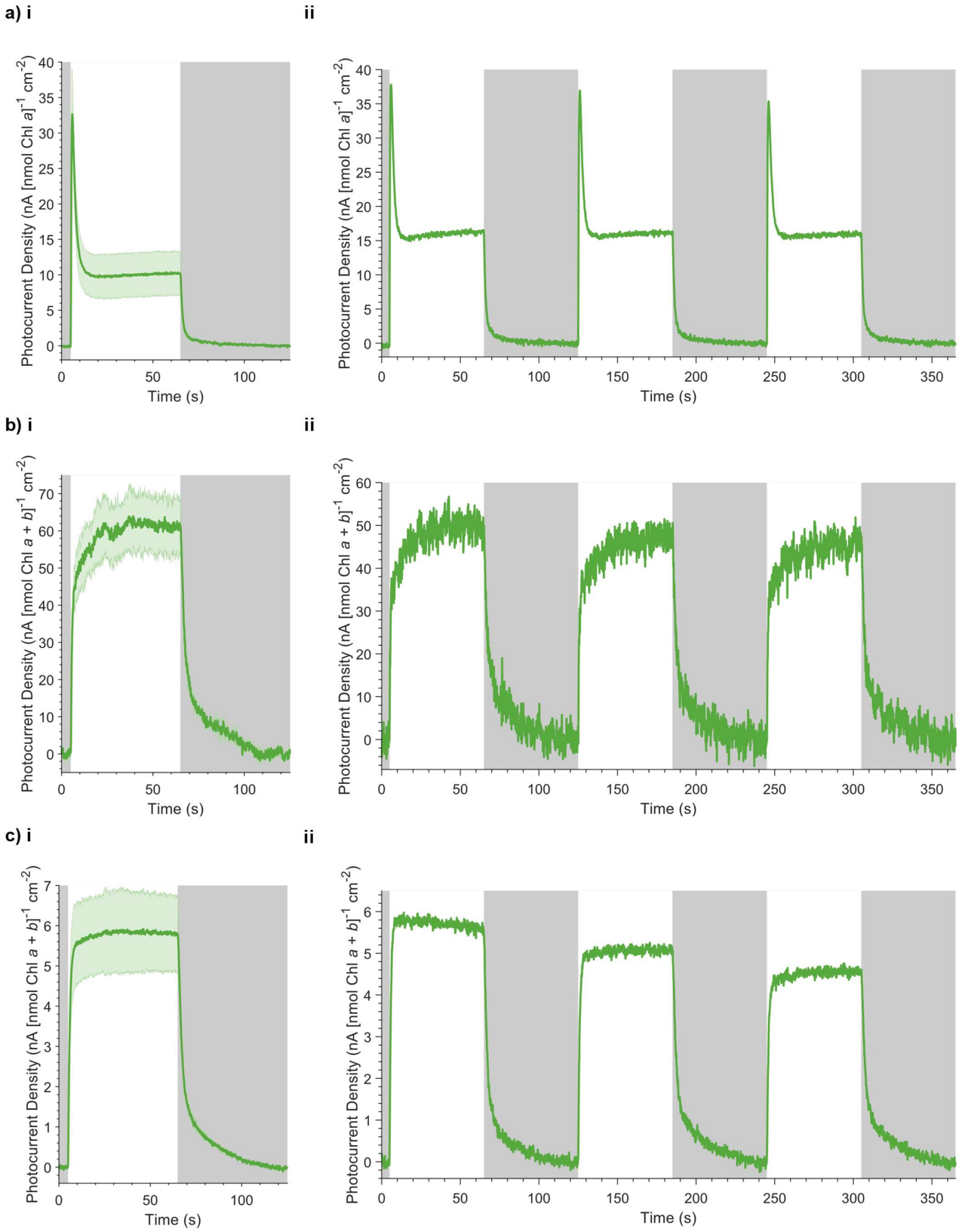

1202

1203 **Extended Data Figure 10: Photocurrent measurements of thylakoid membranes from different**
1204 **species.**

1205 Photocurrents of thylakoid membranes isolated from **a)** *S. elongatus*, **b)** *C. reinhardtii* and **c)** *N.*
1206 *benthamiana*. Sup-panels depict **(i)** the mean of biological replicates ± S.E.M. ($n = 3$), and **(ii)**
1207 representative chronoamperometry scans, depicting successive photocurrent measurements. ($n = 1$).
1208 Chl, chlorophyll.